TÜBİTAK

Turkish Journal of Earth Sciences

http://journals.tubitak.gov.tr/earth/

Research Article

Turkish J Earth Sci
(2019) 28: 38-59

doi:10.3906/yer-1710-5

U-Pb zircon geochronology, geochemistry, and petrogenesis of the Hamech intrusions in the Kuh-e-Shah volcano-plutonic complex, Eastern Iran

Abbas ETEMADI[1], Mohammad Hassan KARIMPOUR[2,*], Azadeh MALEKZADEH SHAFAROUDI[2], José Francisco SANTOS[3], Ryan MATHUR[4], Sara RIBEIRO[3]

[1]Department of Geology, Faculty of Science, Ferdowsi University of Mashhad, Mashhad, Iran
[2]Department of Geology and Research Center for Ore Deposit of Eastern Iran, Faculty of Science, Ferdowsi University of Mashhad, Mashhad, Iran
[3]Department of Geosciences, Geobiotec Research Unit, University of Aveiro, Aveiro, Portugal
[4]Department of Geology, Juniata College, Huntington, PA, USA

Received: 05.10.2017 • **Accepted/Published Online:** 28.11.2018 • **Final Version:** 15.01.2019

Abstract: The Hamech area is located in the west of Kuh-e-Shah volcano-plutonic complex, close to the boundary between the Lut Block and Sistan Suture Zone (SSZ), and is composed of monzonite to diorite porphyries and rare gabbro that intruded into older volcanic rocks. U-Pb zircon dating indicates an age of 36.9 ± 1 Ma for gabbro (Late Eocene, Priabonian) and 38.6 ± 0.5 Ma for dacite (Late Eocene, Bartonian). Geochemically, the studied intrusions are dominantly I-type, high-K calc-alkaline, and metaluminous features. Primitive mantle-normalized trace-element spider diagrams of these rocks present enrichment in ion lithophile elements such as Cs, Rb, Ba, K, and Sr and depletion in high field strength elements such as Nb, Ti, Zr, and heavy rare earth elements. Besides, chondrite-normalized rare earth elements plots of the rocks show enrichment in light rare earth elements ($6.85 < La_N/Yb_N < 9.72$) and a lack or weak negative Eu anomaly ($Eu/Eu^* = 0.81–1.02$). The initial $^{87}Sr/^{86}Sr$ and $^{143}Nd/^{144}Nd$ ratios for the rocks from 0.704541 to 0.704880 and from 0.512633 to 0.512691, respectively, when recalculated to an age of 39 Ma. The $\varepsilon Nd_{(i)}$ values vary from +0.87 to +1.99, which fits into a suprasubduction mantle wedge source for the parental melts. All data suggest that the Hamech intrusions developed in a low maturity continental margin arc setting related to the convergence of the Afghan and Lut Blocks and subduction of Sistan oceanic crust during the Eocene.

Key words: Petrogenesis, U-Pb zircon geochronology, Sr-Nd isotope characteristics, tectonic setting of intrusions, Hamech, Kuh-e-Shah complex

1. Introduction

The tectonic unit of eastern Iran, namely the Lut Block and the Flysch Zone, represent a complex tectonic history related to the evolution of the Sistan Ocean. The Lut Block, as the main body of eastern Iran, confined by faults, extends for about 900 km in the N–S direction (Stocklin and Nabavi, 1973) and only 200 km wide in the E–W direction. The Lut Block is composed of volcanic, volcaniclastic, subvolcanic, and intrusive rocks. The geological history of the Lut Block is characterized by magmatic activities from Middle Jurassic (the S-type Shah-Kuh granitoids; 165-162 Ma) to Cenozoic oceanic island basalts (15.5–1.74 Ma); thus, igneous rocks cover over half of this zone with up to 2000-m thickness (Karimpour et al., 2011). Meanwhile, Tertiary period (42–33 Ma) has a special importance in terms of magmatism and mineralization (Karimpour et al., 2011; Abdi and Karimpour, 2013; Arjmandzadeh and Santos, 2014; Malekzadeh Shafaroudi et al., 2015; Miri Beydokhti, 2015; Samiee et al., 2016; Zirjanizadeh et al., 2016; Hosseinkhani et al., 2017).

The Hamech area is located at the eastern part of the Lut Block (Figure 1) and the western terminal of the Kuh-e-Shah volcano-plutonic complex, which is currently known as one of the most important zones with porphyry type mineralization related to the activity of the Paleogene intrusive-subvolcanic rocks. Considering the position of the study area in the Kuh-Shah complex, the purpose of this paper is: 1) to discuss petrography of intrusive rocks and 2) to discuss more and new geochemical data (major oxides, trace elements, and rare earth elements), Sr-Nd isotopes, and zircon U-Pb data. By this means, we can establish tighter constraints to the discussion about petrogenesis and geodynamic evolution of intrusive rocks in the Hamech area, Kuh-e-Shah volcano-plutonic complex.

* Correspondence: karimpur@um.ac.ir

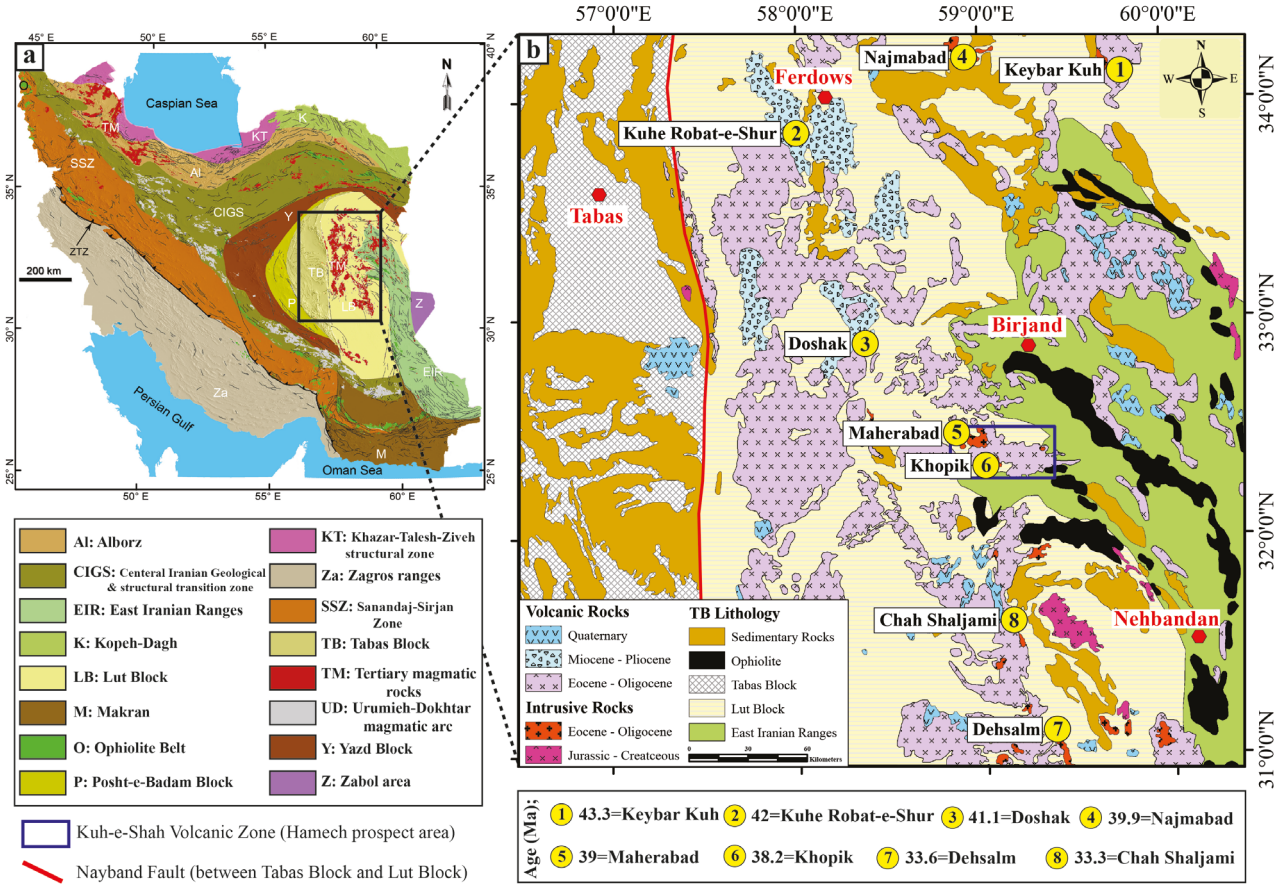

Figure 1. (a) Simplified structural map of Iran (Aghanabati, 1998; Rajabi et al., 2014) and location of the Lut and Tabas Blocks in Central Iranian Microcontinent (CIM). (b) Regional geologic map of eastern Iran (Mahdavi et al., 2016) along with the position of Kuh-e-Shah volcano-plutonic complex, at the east of the Lut Block. Eastern Iran igneous rocks and ophiolite outcrops are shown with red and black colors, respectively. Description: Kaybar Kuh, 43.3 Ma (Salati et al., 2012); Kuh-e-Robat-e-Shur, 42 Ma (Jung et al., 1983); Doshak, 41.1 Ma (Jung et al., 1983); Najmabad, 39.9 Ma (Moradi et al., 2011); Maherabad, 39 Ma (Malekzadeh Shafaroudi, 2009); Khopik, 38.2 Ma (Malekzadeh Shafaroudi et al., 2015); Dehsalm, 33.6 Ma (Arjmandzadeh, 2011); Chah-Shaljami, 33.3 Ma (Arjmandzadeh, 2011).

2. Geological setting and local geology

On a global scale, Iran is situated in the middle part of the Alpine–Himalayan orogenic belt that represents the great Tethys Sea during the Paleozoic–Mesozoic eras (Ghorbani, 2013). Based on the structural classification of Iran (Berberian, 1981; Alavi, 1991; Aghanabati 1998, 2005), Iran is divided into several structural units (Figure 1) and the eastern part of the Central Iran is divided into two parts. A strongly folded eastern part which is named Flysch zone (e.g., Eftekharnezhad, 1980; Ghorbani, 2013) and a western part that is called the Lut Block (Stocklin et al., 1968). The Lut Block is surrounded by faults over some 900 km in the N–S direction and only 200 km wide in the E–W direction. The Hamech area is situated in the western part of Kuh-e-Shah volcanic-plutonic complex and eastern part of the Lut Block, where volcanic and subvolcanic rocks of Tertiary age cover over half of this zone due to the subduction prior to the collision of the Arabian and Asian plates (Camp and Griffis, 1982; Tirrul et al., 1983; Berberian et al., 1999).

The geology of the Hamech area according to the detailed field and petrographic observations can be divided into four sections (Figure 2): 1) Paleocene-to Middle Eocene-aged folded volcaniclastic and sedimentary sequences are composed of conglomerate, shale, sandstone, and tuff breccia. They outcropped in the southeast border of the study area. These lithologies are the oldest units in the Kuh-e-Shah volcanic-plutonic complex and have restricted outcrops in the southern part of altitudes and the Hamech area. In some parts, layering can be seen in sedimentary units and usually tuff breccia covers between them. Moreover, volcanic rocks do not have exposure in this part and exposure features and contact relationships between folded volcaniclastic and sedimentary sequences with intrusive rocks confirm their relative age (Figure 3a); 2) The western part of the

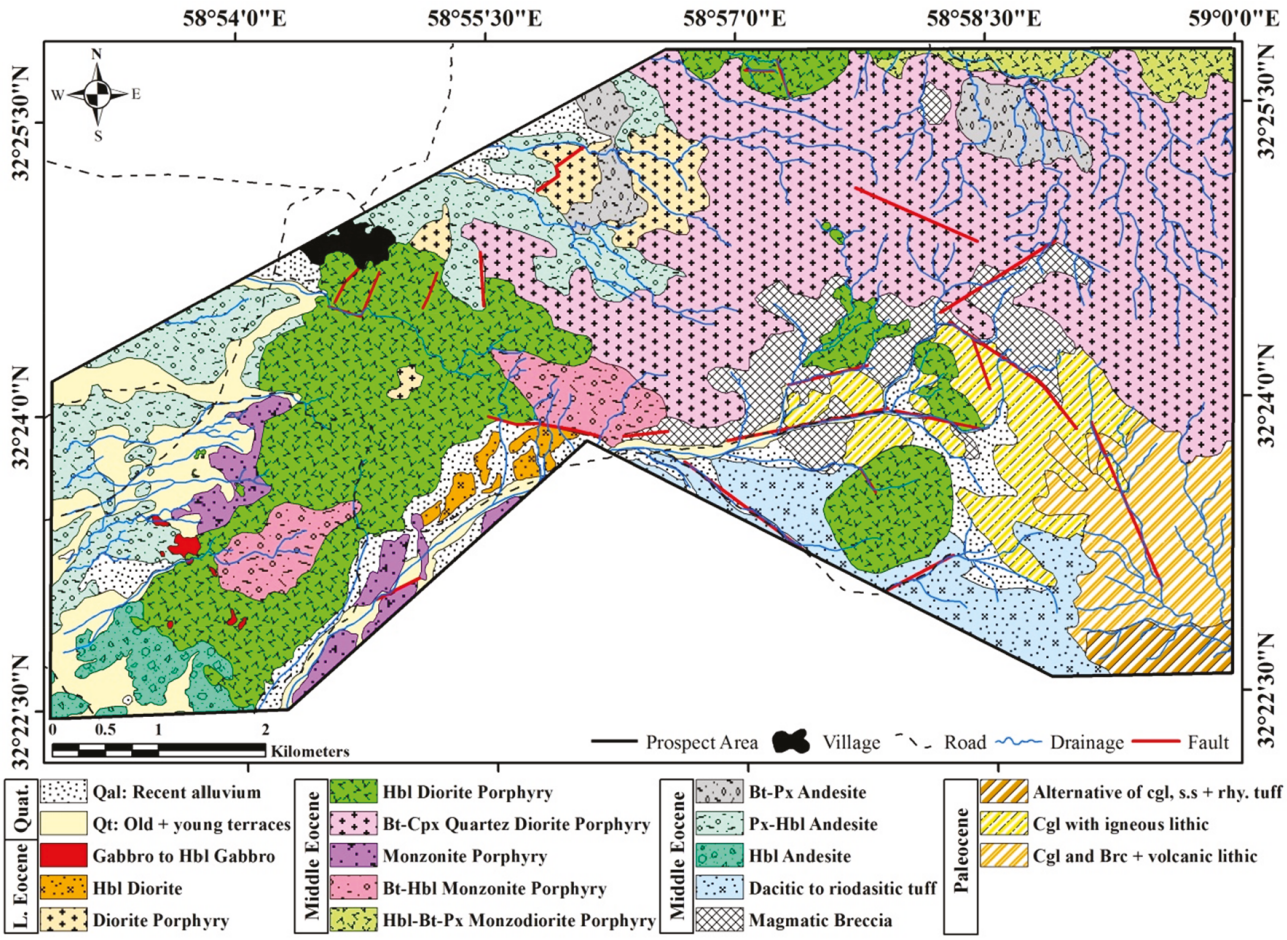

Figure 2. Geological map of the Hamech area (scale 1:20,000). Abbreviations: Hbl: Hornblende, Bt: Biotite, Cpx: Clinopyroxene, Px: Pyroxene (Whitney and Evans, 2010), and Quat.: Quaternary, L. Eocene: Late Eocene, Cgl: Conglomerate, S.S: Sandstone, Rhy.: Rhyolite, Brc: Breccia.

study area (from south to west and northwest) is covered by Middle to Late Eocene-aged intermediate volcanic and pyroclastic rocks including andesite to trachy-andesitic lava, agglomerate, andesitic, dacitic, and rhyodacitic tuff and tuff. They have hill-shaped outcrops and their contact relationships with intrusive rocks well illustrate that they are older (Figure 3b); 3) Late Eocene to Early Oligocene mafic to intermediate intrusive rocks that have intruded into the volcanic units as stocks with granular to porphyry texture and composition of gabbro to diorite, diorite to monzonite porphyry, and monzodiorite porphyry. They cover a major part of Kuh-e-Shah and the Hamech area and form altitudes in an E–W direction (Figure 3c); and 4) Quaternary sediments including old and young terraces, recent alluvium, and gravel fans that covered most of the volcanic units in the south to west lowlands of the study area. In some parts, young conglomerate can be seen as a horizontal layer on the other older units, especially volcanic rocks (Figures 3b and 3d).

3. Material and methods

According to petrographic studies, among the samples with the minimum alteration, 13 low-altered samples from the studied intrusions were selected and analyzed for whole-rock major elements by wavelength-dispersive X-ray Fluorescence (XRF) spectrometry using fused discs at Amethyst Laboratory in Mashhad, Iran. The XRF method is fast, accurate, and nondestructive, and usually requires only a minimum sample preparation. The concentration range goes from (sub) ppm levels to 100%. Generally speaking, the elements with high atomic numbers have better detection limits than the lighter elements. Using the XRF method, we can analyze elements from sodium to uranium but we cannot measure F, O, N, C, B, Be, Li, and H elements. For XRF, detection limits were reported as percentage (%) for major oxides and parts-per-million (ppm) for trace elements.

Refractory and rare earth elements (REEs) were carried out using lithium fusion and inductively coupled plasma

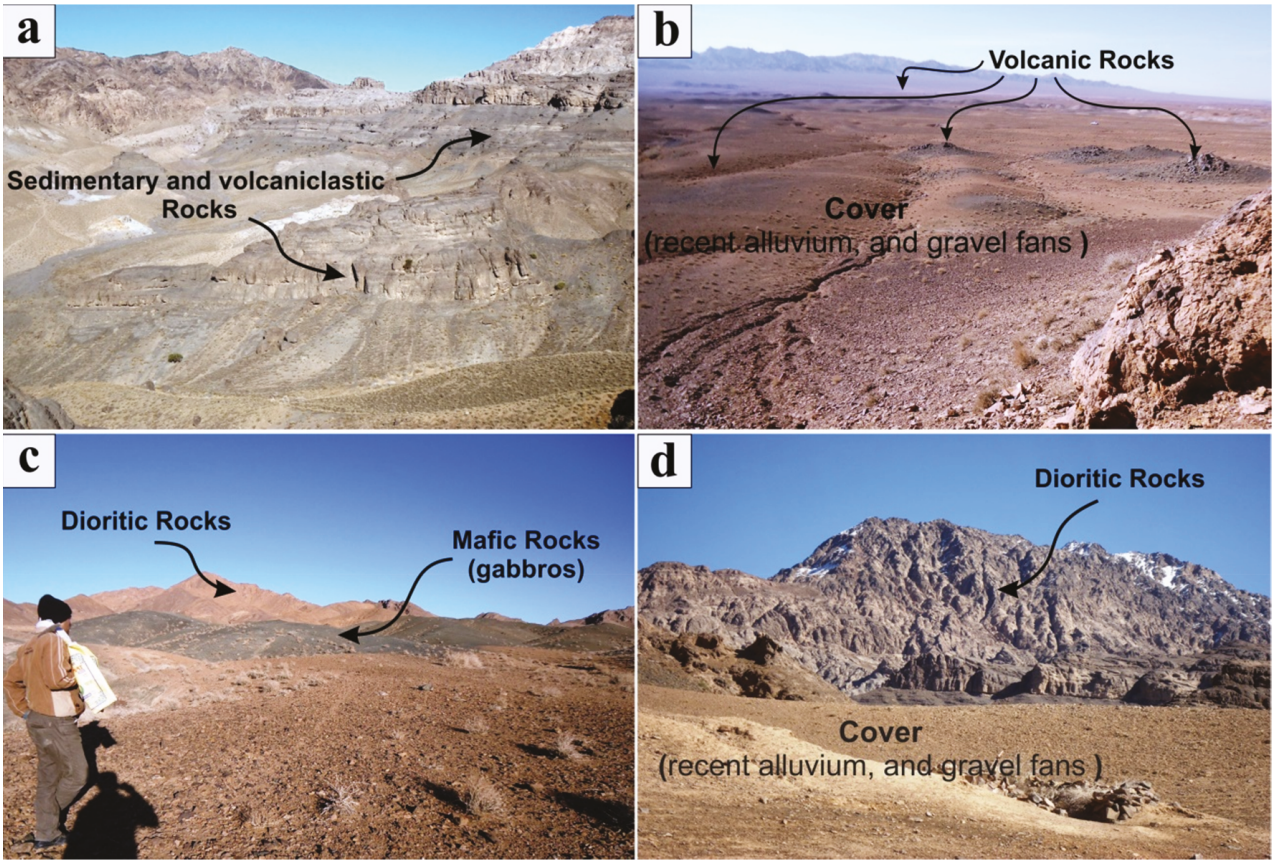

Figure 3. Local geology of the Hamech area including: a) Paleocene- to Middle Eocene-aged folded volcaniclastic and sedimentary sequences; b) Middle to Late Eocene-aged intermediate volcanic and pyroclastic rocks including andesite to trachy-andesitic lava, agglomerate, andesitic, dacitic, and rhyodacitic tuff and tuff; c) Late Eocene to Early Oligocene mafic to intermediate intrusive rocks; d) Quaternary sediments including old and young terraces, recent alluvium, and gravel fans.

mass spectrometry (LF100-ICP-MS) analysis, following a lithium metaborate/tetraborate fusion and Aqua Regia digestion, in the ACME Laboratories, Vancouver, Canada. This method offers increased sensitivity for REEs and trace elements occurring at low concentration levels (Cs, Ta, Th, U, Hf), with detection limits of around 0.01 ppm. ICP-MS is applicable to the determination of sub-µg/L concentrations of a large number of elements. Acid digestion is required prior to filtration and analysis. In LF100-ICP-MS analysis, detection limits (DLs) change for REEs from 0.01 ppm (Tb, Tm, and Lu) to 0.3 ppm (Nd) and for other trace elements from 0.1 ppm (Rb, Zr, Nb, Y, Cs, Ta, Hf, and U) to 8 ppm (V).

For U-Pb zircon dating, two rock samples were collected from gabbroic intrusions and volcanic units. After crushing and washing, zircon crystals were separated using heavy liquid techniques. Zircon grains were handpicked from each sample under a binocular microscope and then were cast in epoxy, polished to expose the centers of the grains and then cleaned in ultrasonic bath. Prior to the analysis, zircon contents were examined by cathode-luminescence (CL) imaging to study internal structure after carbon coating, using a Tescan CL detector instrument at Juniata College, PA, USA. After CL imaging, the LA-ICP-MS U-Pb analyses were conducted using a New Wave Nd:YAG UV 213-nm laser coupled to a Thermo Finnigan Element 2 single collector, double-focusing, and magnetic sector ICP-MS at the GeoAnalytical Lab, University of Washington, WA, USA. Operating procedures and parameters are similar to those of Chang et al.'s (2006). U-Pb ages were calculated using Isoplot (Ludwig, 2007) in two different ways.

Sr and Nd isotopic compositions were determined for six samples of the Hamech intrusions at the Laboratório de Geologia Isotópica da Universidade de Aveiro, Portugal. The values of Rb and Sm elements had already been determined by the ICP-MS analysis. The powdered samples were dissolved in two three-day steps with HF/HNO_3 and HCl (6.2 N) solution in Teflon PFA screw cap vial (Savilex) at 200 °C temperature, respectively. The

Sr and Nd were separated from the dried sample using conventional ion chromatography technique in two stages; (a) separation of Sr and REE elements in ion exchange column with AG8 50W Bio-Rad cation exchange resin and (b) purification of Nd from other lanthanide elements in columns with Ln (ElChrom Technologies) cation exchange resin. Sr and Nd samples were then loaded on a single Ta filament with H_3PO_4 and a Ta outer side filament with HCl in a triple filament arrangement, respectively. $^{87}Sr/^{86}Sr$ and $^{143}Nd/^{144}Nd$ isotopic ratios were determined using a multicollector thermal ionization mass spectrometer (TIMS) VG Sector 54. The Nd and Sr natural isotopic ratios were normalized for mass fractionation relative to $^{88}Sr/^{86}Sr = 0.1194$ and $^{146}Nd/^{144}Nd = 0.7219$. The SRM-987 standard gave an average value of $^{87}Sr/^{86}Sr = 0.710268 \pm 13$ (N = 15; conf. lim = 95%, 2σ) and $^{143}Nd/^{144}Nd = 0.5120985 \pm 53$ (N = 11; conf. lim = 95%, 2σ) to JNdi-1 standard during this study.

4. Results

4.1. Petrography

The studied intrusive rocks are mostly gabbro, hornblende diorite, diorite porphyry, hornblende diorite porphyry, biotite-clinopyroxene quartz diorite porphyry, monzonite porphyry, biotite-hornblende monzonite porphyry, and hornblende-biotite-pyroxene monzodiorite porphyry (Figure 2). The characteristics of the main rocks are as follows.

4.1.1. Gabbroic rocks

According to exposure features and contact relationships observed in the field, the gabbro units are the youngest intrusive rocks in the Hamech area. The gabbroic rocks have an intergranular texture and minerals including 45–50 vol.% plagioclase (0.5–2 mm), 30–32 vol.% green hornblende with euhedral-subhedral shapes (0.3–1.5 mm), 10–12 vol.% needle-shaped actinolite (0.1–0.5 mm), and 5–7 vol.% pyroxene (0.5–0.6 mm). Mineralogically, these units are divided into gabbro and hornblende gabbro. Plagioclases are labradorite type and have low alteration. The rocks are greenish brown in hand samples and some of them contain weak silicification (as very small quartz grain in the matrix) and propylitic (very rare epidote + chlorite + calcite) alteration (Figure 4a).

4.1.2. Dioritic rocks

Diorite porphyry, hornblende diorite porphyry, biotite pyroxene, and quartz diorite porphyry are most widely exposed intrusions in the middle part of the Hamech area. They look like stocks intruded into older lithologies, including volcanic and other intrusive rocks that mainly form altitudes. The dioritic rocks (Hornblende diorite) mainly consist of 65–70 vol.% plagioclase (0.5–3 mm), 15–20 vol.% hornblende (0.5–0.7 mm) and minor amounts of other minerals such as 1–3 vol.% biotite (0.5–0.7 mm), 1–3 vol.% pyroxene (0.5 mm), and a trace of opaque minerals. Most of the plagioclases are oligoclase and are slightly altered to kaolinite, sericite, and carbonate. Hornblendes mostly are green to brownish, green with euhedral shape, and altered to Fe-oxides and opaque mineral along with the minor amounts of chlorite, epidote, and carbonate (Figure 4b).

Other dioritic rocks (diorite porphyry to quartz diorite porphyry) typically contain as much as 50-55 vol.% phenocrysts and the main constituent is plagioclase (oligoclase) with 40–45 vol.% abundance and 0.5 to 1.2 mm thickness. Hornblende, pyroxene, biotite, and quartz are the other rock components whose quantities change between 2 to 10 vol.% and which have the main role in rock classification. In hornblende diorite porphyry, for example, hornblende content reaches 10 vol.% (Figure 4c). Matrix of these rocks is mainly composed of plagioclase microcrystals and quartz, in the case of quartz diorite porphyry. Plagioclase is moderately altered to kaolinite, sericite, and carbonate in the quartz diorite porphyry and strongly altered in the hornblende diorite porphyry. Hornblende and quartz diorite porphyry show moderate silicification to quartz-sericite-pyrite (QSP) alteration.

4.1.3. Monzonitic rocks

The monzonite rocks have porphyritic texture, and mineralogically, are divided into monzonite porphyry, biotite-hornblende monzonite porphyry, and hornblende biotite pyroxene monzodiorite porphyry. The phenocrysts mainly consist of 20%–25% plagioclase (0.5–1.5 mm), 12–15 vol.% K-feldspar (0.5–1 mm), and minor amounts of other phenocrysts including 8–10 vol.% hornblende (0.5–1 mm), 4–5 vol.% biotite (0.7 mm), and 3–4 vol.% pyroxene (0.7 mm) (Figure 4d). Plagioclases change in composition from oligoclase to andesine and are slightly altered to quartz, sericite, and carbonate. The matrix has the same combination with main phenocrysts. Alteration varies from moderate silicification to moderate quartz-sericite-pyrite (QSP) in these units.

4.2. U-Pb zircon geochronology

Among the Hamech igneous rocks, two representative samples were chosen from mafic bodies (73E; gabbro) and volcanic units (28E; dacite) for zircon U-Pb dating. The dacite sample zircons (28E) are white to colorless, amorphous to an elliptical shape, small to large in size (50–250 μm), and show good oscillatory zoning in CL images, suggesting a magmatic origin (Figure 5a). Zircons in the gabbro sample (73E) have similar characteristics (Figure 5b). More than 100 zircon grains of the dacite sample and about 50 zircon grains from the gabbro sample were selected for LA-ICP-MS U-Pb zircon dating that provided 30 and 34 data points, with the weighted mean age being 36.9 ± 1.0 Ma (errors shown are 2σ) for gabbro

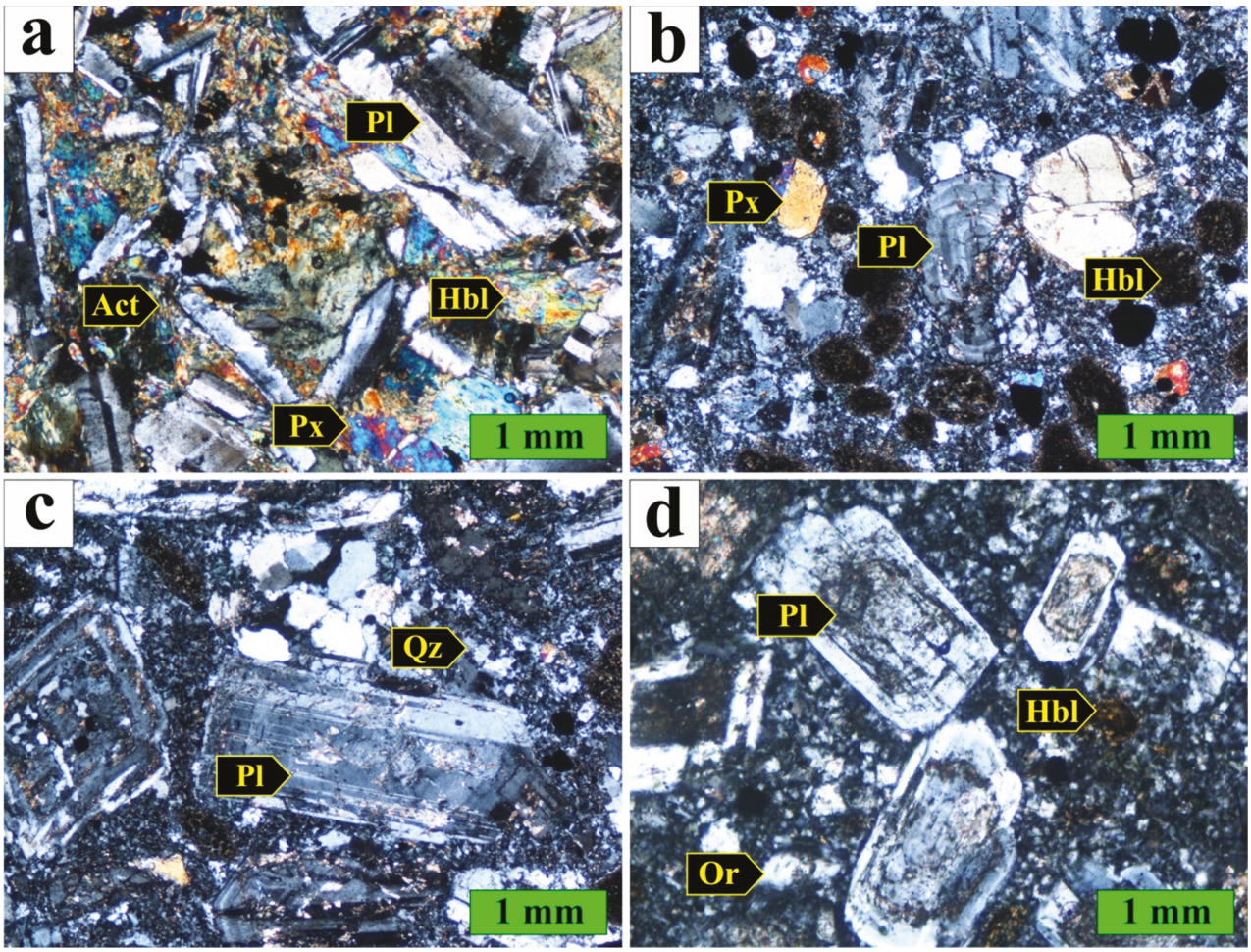

Figure 4. Polarizing microscope images from intrusive units of Hamech area. (a) Gabbro, (b) Diorite, (c) Diorite porphyry, (d) Monzodiorite porphyry. (Abbreviations: Qz: Quartz, Pl: Plagioclase, Hbl: Hornblende, Px: Pyroxene, Act: Actinolite, Or: Orthoclase) (Abbreviations have been taken from Whitney and Evans, 2010).

zircons and 38.6 ± 0.5 Ma (errors shown are 2σ) for dacite zircons, respectively (Table 1). The dating of intrusive rocks in different parts of the Kuh-e-Shah complex (Malekzadeh Shafaroudi, 2009, Abdi and Karimpour, 2013; and Samiee et al., 2016) shows an age range of 31 to 39.7 Ma (Table 2).

The calculation results of the isotopic ages are presented as TuffZirc graphics and Concordia diagrams (Figures 6a, 6b; 73E-gabbro and Figures 6c and 6d; 28E-dacite). Contrary to the dacite example, where zircons indicate a range age from 36.0 to 54.1 Ma, ages more than 100 Ma (up to 2417 Ma; Table 1) were observed in the gabbro sample.

4.3. Whole-rock geochemistry

4.3.1. Major element geochemistry

For geochemical investigation, more than 200 rock samples were taken from the unaltered outcrops available at each locality. After petrography, the best samples were chosen to study chemical characteristics of the intrusive plutons. The representative whole rock major and trace elements of the Hamech intrusions are given in Table 3. The SiO_2 content of the samples ranges from 56.62 to 60.83 wt.% and 45.90 to 51.80 wt.% for intrusions and gabbroic rocks, respectively. The samples exhibit a range in loss-on-ignition (LOI) content from approximately 1.37% to 3.41% (Table 3). That LOI of some samples are more than 2% implies an alteration affect which is also seen in petrography. Also, the K_2O + Na_2O content changes from 5.60 to 7.35 wt.% for intrusions and 2.68 to 2.94 wt.% for gabbroic rocks. Based on the total alkali vs. silica (TAS) diagram of Middlemost (1985), samples in the plot are situated in the field of monzonite, diorite, gabbro, and gabbroic diorite (Figure 7a). As mentioned in the petrography section, what is plotted in the field of gabbroic diorite is gabbro, which is slightly silicified. The values of ASI (alumina saturation index) < 1 and A/NK > 1 for all Hamech intrusions indicate their metaluminous origin and I-type granitoids (Figure 7b; Shand, 1949).

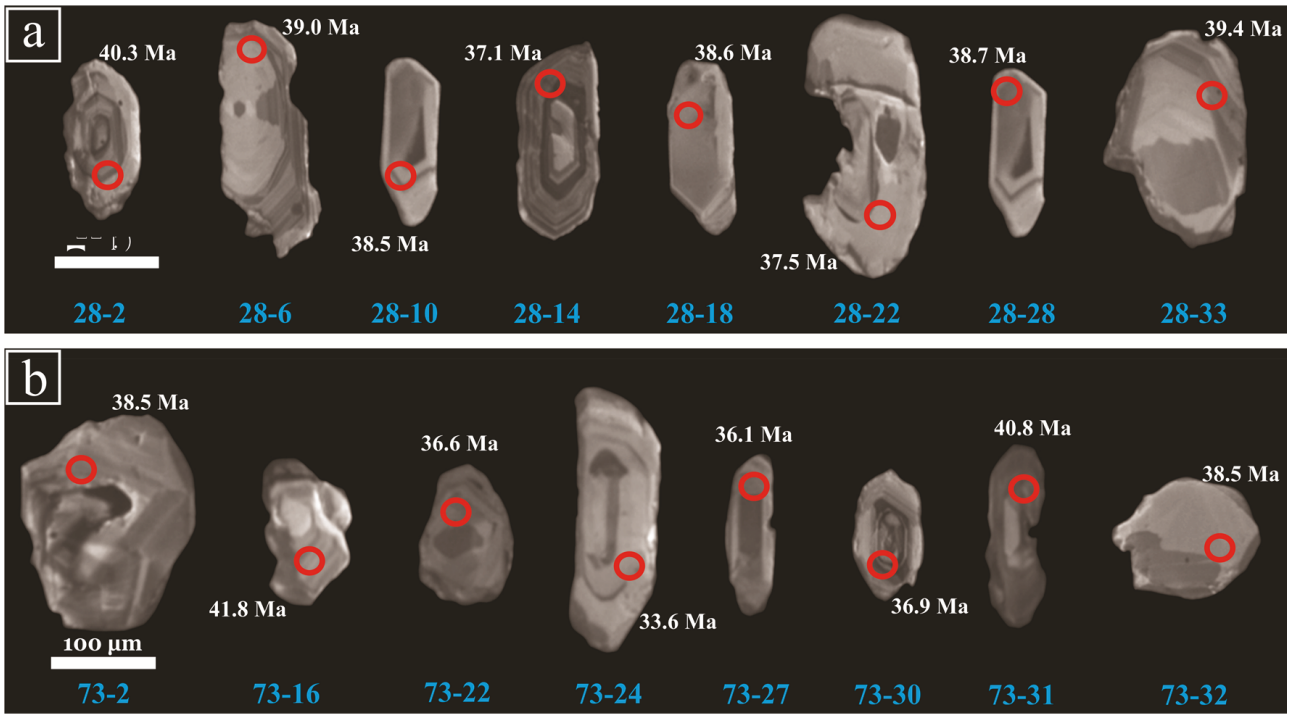

Figure 5. Cathodo-luminescence images of representative zircon grains from (a) 28E-dacite and (b) 73E-gabbro. The red circles show approximate location of laser ablation spots and are not to scale.

Using the K_2O vs. SiO_2 nomenclature of Peccerillo and Taylor (1976), the diorites and monzonites are classified as high-K (K_2O between 2.42 and 4.0 wt.%) and the gabbro bodies in the tholeiitic magma series (K_2O between 0.15 and 0.27 wt.%) (Figure 7c). Plots of major elements vs. SiO_2 of the Hamech dioritic and monzonitic rocks are shown in Figure 8. In these major element diagrams, SiO_2 shows a negative correlation with TiO_2, Fe_2O_3, MnO, MgO, CaO, and P_2O_5 and a positive correlation with Na_2O, K_2O, and Al_2O_3, which suggests that fractional crystallization has been affected during magmatic evolution.

4.3.2. Trace element geochemistry

In order to study the trace element geochemistry of the Hamech intrusive rocks, thirteen selected samples were analyzed from to different groups of rocks, gabbroic and dioritic type, by ICP-MS (Table 3).

Trace elements were normalized to primitive mantle (Sun and McDonough, 1989; Figure 9a) for dioritic and monzonitic rocks and gabbroic rocks. The intermediate and mafic intrusive rocks show different patterns. Results show that the dioritic rocks display similar averaged values of trace elements higher than those of gabbroic types. A significant negative anomaly of high field strength elements (HFSE) such as Nb, Ti, Ta, Zr, and Y and a positive anomalies of large ion lithophile elements (LILE) such as Cs, Rb, Ba, K, Th, and U are characteristics of the magmas associated with subduction zones (Wilson, 1989).

Chondrite-normalized REEs (Boynton, 1985) of the Hamech intrusions are given in Figure 9b. The REEs' patterns in dioritic and monzonitic rocks, unlike gabbroic rocks, show a moderate enrichment of light rare earth elements (LREE) relative to heavy rare earth elements (HREE). The La_N/Yb_N and Ce_N/Yb_N change from 6.85 to 9.72 and from 4.87 to 7.07 in the dioritic and monzonitic rocks and from 0.46 to 0.80 and from 0.52 to 0.78 in gabbroic rocks, respectively (Table 3). The Eu/Eu* ratio varies from 0.81 to 1.06 in all of the intrusive rocks, suggesting a lack or inconsiderable negative anomaly.

Even though the diagrams of Harker show a scattered distribution of trace elements when plotted against SiO_2 contents (Figure 10), some linear trends can be traced. Different linear trends distinctly separate rocks of the dioritic suite from those of the gabbroic one (including two samples of gabbro and gabbroic diorite) especially in the SiO_2 vs. Rb, Sr, Ba, or La diagrams. The trends are, however, consistent with the results of the major-element statistical test in showing that the intrusive rocks are similar in their elemental concentrations but not identical. Very low Rb/Sr ratio in the gabbroic (0.03 to 0.05) and dioritic rocks (0.05 to 0.11) documents primitive source of rocks.

4.4. Sr-Nd isotopes

The $^{87}Sr/^{86}Sr$ and $^{143}Nd/^{144}Nd$ isotopic ratios of the Hamech intrusive rocks are summarized in Table 4. The initial $^{87}Sr/^{86}Sr$ and $^{143}Nd/^{144}Nd$ ratios of diorite and monzonite

Table 1. U-Pb zircon geochronology data of samples from Hamech study area. 28E: Dacite and 73E: Gabbro.

Sample no.	^{238}U ppm	U/Th ppm	$^{207}Pb/^{235}U$	2s	$^{206}Pb/^{238}U$	2s	Corr. Coef.	$^{238}U/^{206}Pb$	2s	$^{207}Pb/^{206}Pb$	2s	Age	±Ma
28 E: Dacite													
28-1	407	2.5	0.04097	0.00337	0.00622	0.00027	0.724	160.7030	7.0552	0.0478	0.0028	39.9	1.8
28-2	273	2.4	0.07253	0.00548	0.00627	0.00028	0.739	152.6236	6.4206	0.0803	0.0042	40.3	1.7
28-3	211	2.7	0.03147	0.00326	0.00598	0.00028	0.686	169.0564	7.9114	0.0386	0.0031	38.4	1.8
28-4	410	2.7	0.03893	0.00319	0.00597	0.00025	0.716	167.3113	7.0484	0.0472	0.0028	38.4	1.6
28-5	197	2.9	0.03900	0.00365	0.00594	0.00028	0.703	168.0649	7.8127	0.0476	0.0033	38.2	1.8
28-6	151	2.1	0.04488	0.00618	0.00606	0.00033	0.666	163.5342	8.8190	0.0532	0.0058	39.0	2.1
28-7	550	2.7	0.03865	0.00267	0.00601	0.00024	0.753	166.4758	6.6094	0.0467	0.0022	38.6	1.5
28-8	1291	4.1	0.03874	0.00217	0.00591	0.00021	0.807	169.0317	6.1265	0.0475	0.0016	38.0	1.4
28-9	120	2.3	0.04005	0.00581	0.00623	0.00033	0.665	160.5794	8.6264	0.0467	0.0054	40.0	2.2
28-10	349	2.5	0.03722	0.00309	0.00600	0.00025	0.712	167.1356	6.9738	0.0451	0.0027	38.5	1.6
28-11	158	3.3	0.04090	0.00434	0.00609	0.00030	0.687	163.8604	7.9877	0.0486	0.0039	39.1	1.9
28-12	448	2.3	0.05048	0.00435	0.00593	0.00034	0.778	165.6882	9.2792	0.0607	0.0034	38.1	2.1
28-13	133	2.1	0.10352	0.00975	0.00623	0.00039	0.755	147.4419	8.5318	0.1107	0.0070	40.0	2.3
28-14	1302	3.0	0.03748	0.00263	0.00577	0.00027	0.799	173.2524	8.1365	0.0471	0.0020	37.1	1.7
28-15	211	2.3	0.03980	0.00387	0.00622	0.00031	0.707	160.9477	7.9728	0.0465	0.0033	39.9	2.0
28-16	162	1.9	0.04395	0.00525	0.00613	0.00034	0.684	162.1605	9.0353	0.0517	0.0047	39.4	2.2
28-17	173	2.1	0.03987	0.00503	0.00590	0.00032	0.675	169.0511	9.2604	0.0489	0.0048	37.9	2.1
28-18	625	2.0	0.03899	0.00252	0.00601	0.00022	0.759	166.4553	6.2015	0.0471	0.0021	38.6	1.4
28-19	589	2.5	0.04239	0.00274	0.00608	0.00023	0.763	163.7052	6.2000	0.0503	0.0022	39.1	1.5
28-20	871	3.1	0.04144	0.00252	0.00624	0.00023	0.776	159.9050	5.8504	0.0481	0.0019	40.1	1.5
28-21	450	2.5	0.04801	0.00310	0.00600	0.00023	0.766	164.3736	6.2990	0.0572	0.0025	38.6	1.5
28-22	728	2.5	0.03834	0.00220	0.00583	0.00020	0.781	171.3696	5.8929	0.0477	0.0018	37.5	1.3
28-23	186	2.0	0.04317	0.00480	0.00612	0.00028	0.676	162.4976	7.5008	0.0509	0.0044	39.3	1.8
28-24	201	1.2	0.03742	0.00410	0.00610	0.00024	0.676	164.3886	6.5088	0.0446	0.0039	39.2	1.6
28-25	201	2.8	0.05085	0.00547	0.00623	0.00030	0.681	158.2439	7.4307	0.0584	0.0049	40.0	1.9
28-26	415	2.6	0.03754	0.00277	0.00600	0.00025	0.749	167.0013	7.0955	0.0455	0.0023	38.6	1.6
28-27	626	3.1	0.03669	0.00253	0.00585	0.00024	0.764	171.1681	7.0554	0.0456	0.0021	37.6	1.6
28-28	257	2.3	0.03575	0.00371	0.00602	0.00028	0.686	166.9363	7.8638	0.0433	0.0034	38.7	1.8
28-29	603	2.5	0.04143	0.00315	0.00581	0.00026	0.756	171.0078	7.7192	0.0514	0.0026	37.4	1.7
28-30	148	1.9	0.03673	0.00523	0.00600	0.00034	0.666	167.1033	9.5700	0.0445	0.0050	38.6	2.2
28-31	168	2.2	0.03857	0.00482	0.00599	0.00031	0.673	167.0085	8.7703	0.0467	0.0046	38.5	2.0
28-32	295	2.1	0.03701	0.00325	0.00571	0.00023	0.695	175.0670	7.0148	0.0470	0.0031	36.7	1.5
28-33	219	2.4	0.03907	0.00378	0.00612	0.00030	0.707	163.3780	8.0628	0.0463	0.0033	39.4	1.9
28-34	216	2.7	0.03922	0.00427	0.00629	0.00030	0.680	159.2762	7.5230	0.0453	0.0038	40.4	1.9
73 E : Gabbro													
73-1	49	3.3	2.73769	0.12861	0.20387	0.00746	0.891	4.8043	0.1722	0.0954	0.0021	1536.4	20.7
73-2	1319	3.8	0.04483	0.00240	0.00599	0.00021	0.817	165.3678	5.8279	0.0538	0.0017	38.5	1.4
73-3	303	1.4	1.06707	0.04742	0.11904	0.00417	0.912	8.3853	0.2930	0.0649	0.0012	725.0	24.6
73-4	1001	1.1	0.04085	0.00282	0.00640	0.00025	0.753	156.4025	6.1808	0.0464	0.0022	41.1	1.6

Table 1. (Continued).

73-5	813	2.8	1.76639	0.07137	0.17215	0.00538	0.918	5.8012	0.1810	0.0743	0.0013	1050.8	17.1
73-6	804	1.3	9.75988	0.42217	0.45489	0.01607	0.934	2.2003	0.0778	0.1558	0.0025	2417.0	13.7
73-7	426	1.7	0.04318	0.00440	0.00645	0.00033	0.700	154.6366	7.8562	0.0484	0.0037	41.5	2.1
73-8	928	0.8	0.42296	0.01818	0.04822	0.00158	0.896	20.4604	0.6608	0.0628	0.0013	303.6	9.7
73-10	16997	0.6	0.20362	0.00912	0.02427	0.00087	0.911	40.6294	1.4325	0.0600	0.0012	154.6	5.4
73-11	1745	1.0	0.98676	0.04243	0.09955	0.00353	0.933	9.9062	0.3467	0.0709	0.0012	611.8	20.9
73-12	1064	1.6	0.10846	0.00501	0.01609	0.00054	0.870	62.0943	2.0710	0.0489	0.0012	102.9	3.4
73-13	953	1.3	0.22793	0.01633	0.01604	0.00074	0.763	58.4763	2.5201	0.0967	0.0046	102.6	4.4
73-14	1022	1.4	0.10992	0.00600	0.01611	0.00061	0.830	61.9696	2.3245	0.0494	0.0016	103.0	3.8
73-15	1281	1.3	0.07567	0.00354	0.01137	0.00039	0.872	87.8470	2.9943	0.0482	0.0012	72.9	2.5
73-16	942	3.9	0.05945	0.00321	0.00651	0.00022	0.788	150.0861	4.8711	0.0647	0.0022	41.8	1.4
73-17	360	1.2	0.30323	0.01447	0.04280	0.00147	0.863	23.3716	0.8012	0.0514	0.0013	270.2	9.2
73-18	592	1.9	0.05669	0.00327	0.00855	0.00031	0.792	116.7651	4.1978	0.0480	0.0018	54.9	2.0
73-19	308	3.0	0.09776	0.00995	0.00780	0.00062	0.825	121.7234	9.1214	0.0863	0.0050	50.1	3.8
73-20	237	1.6	0.09025	0.00642	0.01191	0.00050	0.758	83.2047	3.4910	0.0545	0.0026	76.3	3.2
73-22	597	3.1	0.05736	0.00466	0.00570	0.00024	0.716	170.1603	7.0503	0.0708	0.0042	36.6	1.5
73-23	2142	0.9	0.51205	0.02077	0.06465	0.00203	0.917	15.4195	0.4826	0.0573	0.0010	403.8	12.4
73-24	1261	1.8	0.03518	0.00195	0.00522	0.00018	0.801	190.8975	6.7150	0.0487	0.0017	33.6	1.2
73-26	966	0.2	4.79859	0.19069	0.29102	0.00938	0.933	3.3618	0.1060	0.1170	0.0018	1911.4	13.7
73-27	282	2.5	0.04746	0.00550	0.00561	0.00029	0.677	175.1509	8.7491	0.0603	0.0054	36.1	1.8
73-28	428	2.5	0.95982	0.04046	0.10504	0.00350	0.919	9.4611	0.3136	0.0659	0.0012	643.9	20.8
73-29	876	3.9	0.86487	0.03536	0.10137	0.00321	0.916	9.8487	0.3113	0.0618	0.0011	622.4	19.2
73-30	167	1.3	0.06177	0.01198	0.00575	0.00048	0.510	167.7420	13.5771	0.0752	0.0126	36.9	3.0
73-31	133	1.1	0.10460	0.01623	0.00635	0.00042	0.497	144.7681	8.7586	0.1099	0.0149	40.8	2.6
73-32	144	1.3	0.04511	0.00598	0.00599	0.00036	0.540	165.4594	9.7575	0.0541	0.0061	38.5	2.3

Explanation: Two incorrect data of 73E sample have been deleted and due to the presence of data from wall rock remaining zircons, resulting age for this sample is taken from 5 coherent groups of zircon.

Table 2. The intrusive rocks' ages in the Kuh-e-Shah volcano-plutonic complex, SW Birjand, eastern Lut Block (1-Malekzadeh Shafaroudi, 2009, 2-Abdi and Karimpour, 2013; and 3-Samiee et al., 2016) together with the new data obtained from intrusive and volcanic rocks of the Hamech area. Abbreviations: Hbl: hornblende, Bt: biotite, Qz: quartz, Px: pyroxene (Whitney and Evans, 2010).

Location	Maherabad[1]	Khopik[1]	Kuh-e-Shah[2]		Khunik[3]		Hamech	
Sample no.	MA-126	KH-88	Bd4	G44	Kh-366	kh-317	73E	28E
Rock type	Hbl monzonite	Hbl monzonite	Qz diorite porphyry	Qz diorite porphyry	Px-diorite porphyry	Bt granodiorite porphyry	Gabbro	Dacite
Age (Ma)	39	38.2	39.7	39.6	38	31	36.9	38.6

rocks vary in a limited range from 0.704541 to 0.704880 and from 0.512633 to 0.512691 (Table 4), respectively, when recalculated to an age of 39 Ma that is consistent with the new radiometric results. Also, $^{87}Sr/^{86}Sr$ and $^{143}Nd/^{144}Nd$ isotopic ratios in gabbroic rocks range in a wider range from 0.703399 to 0.704704 and from 0.512979 to 0.513013 (Table 4), respectively.

The $\varepsilon Nd(i)$ varies from +0.87 to +1.99 in intermediate intrusions and from +7.58 to +8.25 in mafic rocks. The depleted mantle Nd model ages (TDM) was calculated

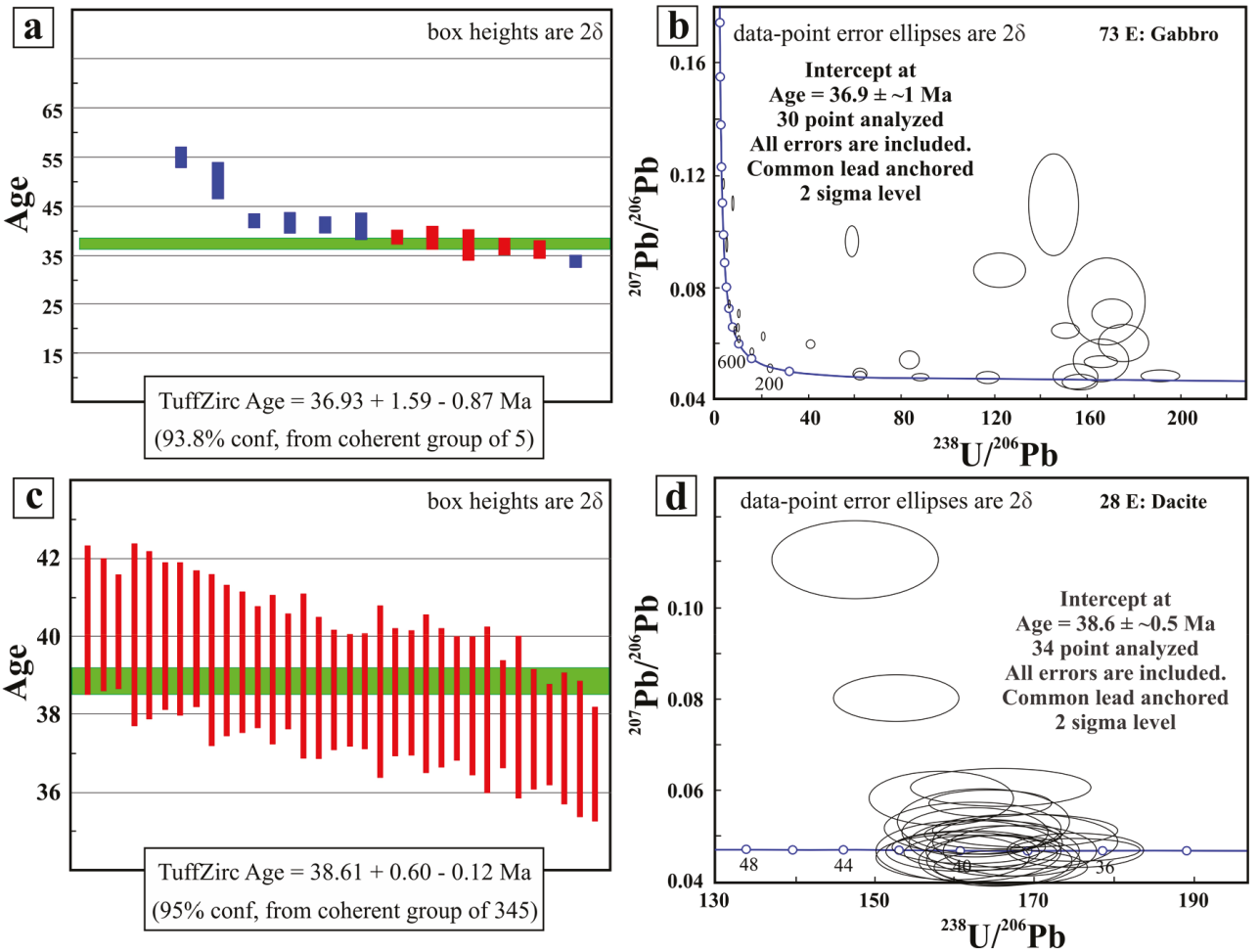

Figure 6. (a) TuffZirc plot showing zircon ages for 73E-gabbro sample, (b) Tera-Wasseburg Concordia diagrams of 73E-gabbro sample, (c) TuffZirc plot showing zircon ages for 28E- dacite sample, (d) Tera-Wasseburg Concordia diagrams of 28E-dacite sample.

from the depleted mantle (Liew and Hofmann, 1988) and vary in a limited range of +0.69 to +0.78 Ga for intermediate intrusions and +0.17 to +0.23 for mafic rocks. In the ƐNd(i) vs. ($^{87}Sr/^{86}Sr$)i diagram (Figure 11), all samples are plotted slightly to the right of the so-called "mantle array" and near the depleted mantle.

5. Discussion

5.1. Magma source

5.1.1. REE geochemistry

The parallel trend of chondrite-normalized (Boynton, 1984) REEs pattern in intermediate intrusive rocks suggests a similarity of magmatic processes during the formation and difference in their REEs enrichment pattern with the mafic bodies, suggesting their different origin and/or magmatic process during the evolution. The LREE/HREE enrichment in dioritic rocks is an indicator of crustal contamination or melts created in subduction zones by low degrees of partial melting (Zulkarnain, 2009; Helvacı et al., 2009; Nicholson et al., 2004; Asiabanha et al., 2012; Rollinson, 2014). The REE pattern and relatively moderate enrichment of $(La/Yb)_N$ and $(Ce/Yb)_N$ in the intermediate intrusions show that parent magma formed at a shallow depth, outside the stability field of garnet (lack of garnet at the source) or formed by low degrees of partial melting (Defant and Drummond, 1990). These ratios for dioritic rocks are less than those of magmas ($La_N/Yb_N > 20$, e.g., Martin, 1987) whose source contains garnet; therefore, spinel/amphibolite may be present in residual.

The absence or slight negative Eu anomaly ($Eu/Eu^* = 0.81$ to 1.02) could be due to several factors, including (1) nondifferentiation of plagioclase from primary magma; (2) the suspension of plagioclase differentiation due to the high content of magmatic water; (3) presence of Eu mainly as Eu^{3+} at high oxidation conditions; therefore, only small amounts of Eu^{2+} will be available for incorporation

Table 3. Major (wt.%), trace, and rare earth element (ppm) composition of the Hamech intrusive rocks.

Sample	**2-1 E**	**3 E**	**16 E**	**97 E**	**144 E**	**146 E**	**153 E**	**19 E**	**50 E**	**55 E**	**112 E**	**73 E**	**74 E**
Longitude	58°55′1 ″	58°55′11 ″	58°55′11 ″	58°54′31 ″	58°57′29 ″	58°57′32 ″	58°58′9 ″	58°56′10 ″	58°55′3 ″	58°55′14 ″	58°54′57 ″	58°53′35 ″	58°53′41 ″
Latitude	32°24′6 ″	32°23′50 ″	32°23′50 ″	32°23′12″	32°24′10″	32°24′10″	32°23′47″	32°25′3″	32°24′40″	32°24′28″	32°23′23″	32°23′21″	32°23′20″
Rock type	Dio.	Dio.	Dio.	Dio.	Dio.	Dio.	Dio.	Mon.	Mon.	Mon.	Mon.	Gab.	Gab.
wt.%													
SiO_2	60.83	58.65	59.29	58.83	60.08	59.87	57.28	59.79	58.17	56.62	57.23	45.90	51.80
TiO_2	0.54	0.53	0.56	0.60	0.53	0.52	0.56	0.64	0.57	0.57	0.60	0.90	1.17
Al_2O_3	15.10	15.71	16.10	15.78	15.71	15.88	15.37	16.25	16.02	15.48	15.72	13.88	13.31
FeO^t	5.38	6.39	5.96	7.14	5.87	5.62	7.01	5.70	6.48	6.48	6.75	8.93	9.03
MnO	0.12	0.14	0.13	0.13	0.12	0.11	0.14	0.11	0.14	0.13	0.16	0.11	0.16
MgO	3.51	2.94	2.00	3.30	2.97	2.24	3.47	1.21	4.08	5.22	3.05	11.60	8.60
CaO	4.89	6.34	6.90	6.48	5.59	6.31	6.77	6.48	4.88	4.83	6.63	14.12	11.15
Na_2O	3.21	3.13	3.18	3.18	3.49	3.24	3.24	3.35	3.12	3.55	3.85	2.41	2.79
K_2O	3.17	2.48	2.42	2.61	2.63	2.50	2.69	4.00	3.21	3.16	2.58	0.27	0.15
P_2O_5	0.28	0.31	0.34	0.33	0.33	0.33	0.33	0.45	0.32	0.34	0.39	0.07	0.10
LOI	2.74	3.16	2.90	1.37	2.44	3.14	2.92	1.76	2.84	3.41	2.80	1.66	1.63
SUM	99.77	99.78	99.78	99.75	99.76	99.76	99.78	99.74	99.83	99.79	99.76	99.85	99.89
ppm													
Ba	779	619	586	576	931	748	655	696	593	676	517	13	13
Rb	68	61	57	57	55	50	59	92.3	76.2	69.1	53.5	8.7	3.6
Sr	777	822	933	1109	945	903	893	959	665	746	1124	191	143
Zr	96	77	83	78	89	79	81	102.6	70.0	79.4	95.5	33.6	79.4
Nb	3.1	3	3.5	2.5	3	2.5	3.1	4.8	2.4	2.8	3.5	0.5	1.1
Ni	7	11	10	14	8	-	22	7	9	4	-	111	93
Co	13.3	13.3	13.0	17.5	12.3	11.2	16.1	11.7	14	14.9	16.4	39.3	37
Zn	108	99	84	80	82	-	79	65	80	62	80	31	63
Cr	15	23	18	23	14	-	14	3	8	20	17	421	286
Y	15.0	17.3	17.4	18.3	15.4	15.2	18.1	16.4	17.5	16.8	23.3	18.9	26
Cs	7.5	16.3	12	7.9	6.5	8.5	4	4.9	14.9	12.3	8.1	10.1	2
Ta	0.2	0.2	0.2	0.3	0.2	0.2	0.1	0.3	0.2	0.1	0.2	<0.1	<0.1
Hf	2.5	2.1	2.1	2.2	2.3	2.0	2.2	2.7	2	2.3	2.5	1.2	2.2
La	20.7	21.5	21.6	22.9	22.9	21.1	21.4	26.1	19.1	21.6	31.1	1.3	3.3
Ce	39.2	40.0	40.0	41.1	40.9	39.9	40.5	49.5	35.4	41.3	57.6	3.8	8.4
Pr	4.8	5.1	5.2	5.0	5.2	5.0	5.2	6.0	4.5	5.0	7.2	0.7	1.5
Nd	19.1	21.6	22.3	20.7	22.4	20.5	21.6	25.6	18.9	22.9	30.8	3.6	8.4
Sm	4.3	4.4	4.3	4.0	4.2	3.9	4.4	4.9	4.0	4.4	5.7	1.6	2.7
Eu	1.01	1.21	1.24	1.21	1.21	1.19	1.22	1.30	1.12	1.24	1.47	0.69	0.99
Gd	3.32	4.15	3.90	4.13	3.61	3.24	3.95	4.14	3.68	3.87	5.21	2.52	3.72
Tb	0.45	0.58	0.56	0.56	0.48	0.45	0.56	0.55	0.54	0.55	0.68	0.46	0.67
Dy	3.20	3.32	3.29	3.50	2.91	2.77	3.23	3.14	3.16	3.31	4.06	3.41	4.46
Ho	0.59	0.62	0.67	0.73	0.59	0.56	0.65	0.62	0.67	0.62	0.89	0.75	1.02
Er	1.76	2.02	2.01	2.03	1.73	1.51	2.06	1.64	2.06	1.86	2.74	2.00	2.82
Tm	0.25	0.31	0.29	0.30	0.28	0.23	0.29	0.27	0.29	0.29	0.36	0.30	0.41
Yb	1.76	2.09	1.86	2.15	1.90	1.75	1.91	1.81	1.88	1.98	2.58	1.89	2.79
Lu	0.28	0.31	0.36	0.32	0.32	0.26	0.34	0.27	0.31	0.32	0.39	0.32	0.40
$(La/Yb)_N$	7.93	6.94	7.83	7.18	8.13	8.13	7.55	9.72	6.85	7.35	8.13	0.46	0.80
$(Ce/Yb)_N$	5.76	4.95	5.56	4.94	5.57	5.90	5.48	7.07	4.87	5.40	5.77	0.52	0.78
Eu/Eu*	0.81	0.86	0.92	0.91	0.95	1.02	0.90	0.89	0.89	0.92	0.83	1.06	0.96

Eu*: expected concentration by interpolating between the normalized value of Sm and Gd. N: normalized to chondritic meteorite. Eu/Eu* = Eu/√Sm × Gd. Abbreviations: Dio.: Diorite, Mon.: Monzonite, Gab.: Gabbro, LOI: Loss On Ignition.

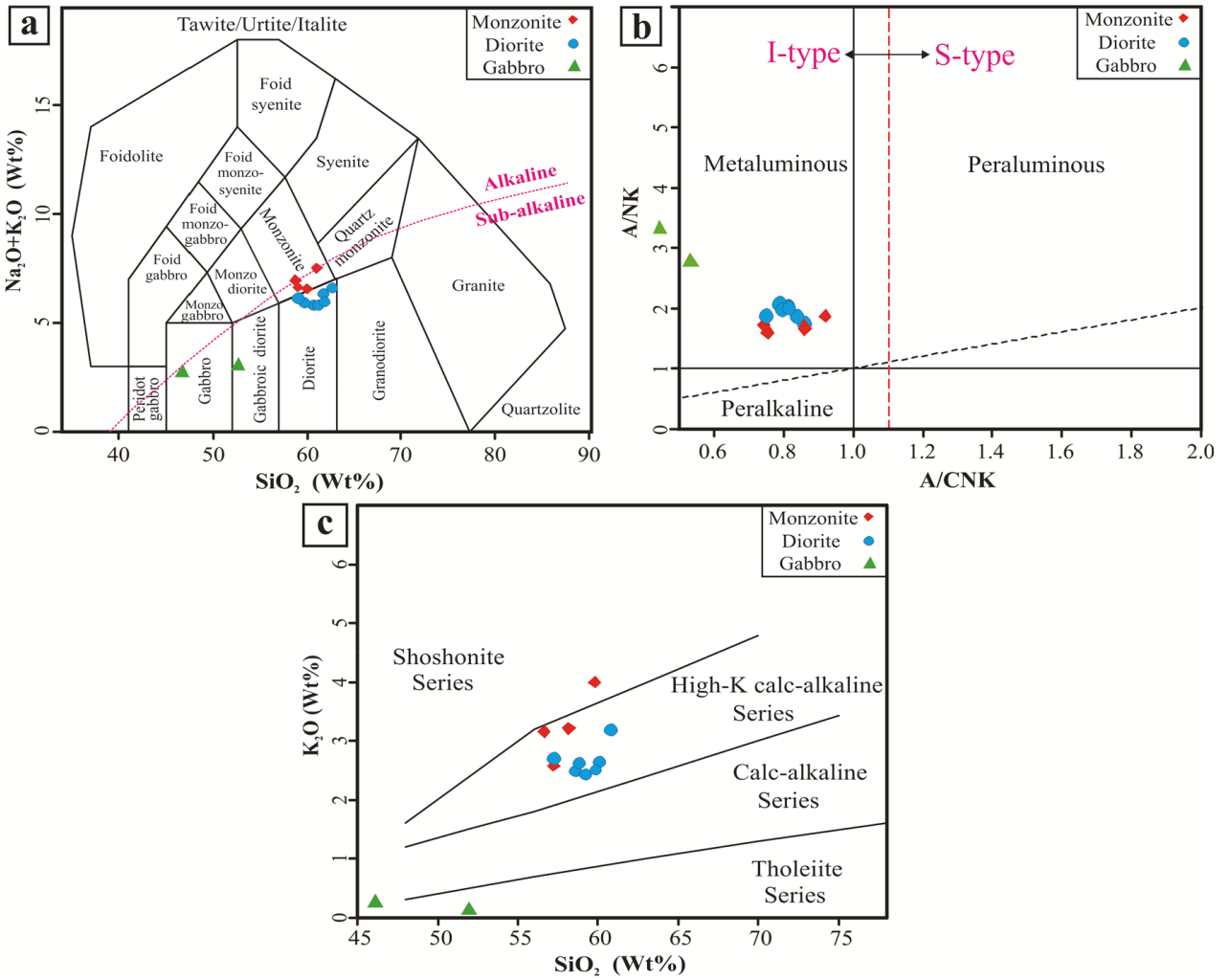

Figure 7. (a) Na_2O+K_2O vs. SiO_2 diagram to classification (Middlemost, 1985), (b) $Al_2O_3/Na_2O + K_2O$ (molar) vs. $Al_2O_3/(CaO + K_2O + Na_2O)$ (molar) diagram (Shand, 1949), (c) K_2O vs. SiO_2 diagram (Peccerillo and Taylor, 1976) for the studied Hamech intrusive rocks.

in plagioclase (Drake and Weill, 1975; Frey et al., 1978; Hanson, 1980; Richards et al., 2012).

In spider diagrams of the primitive-mantle-normalized trace elements (Sun and McDonough, 1989; Figure 9a), it is seen that all of the intrusive rocks are enriched in highly incompatible elements such as LILEs (e.g., Cs, Rb, Ba, K, and Sr), and are depleted in HFSEs (e.g., Nb, Ti, and Zr). This high LIL/HFS pattern is now recognized as a distinctive feature of subduction-related magmas and signature of crustal contamination in the volcanic arcs of continental active margins (Gill, 1981; Pearce, 1983; Rollinson, 1993; Thirlwall et al., 1994; Wilson, 1989; Winter, 2001). Geochemical data such as Nb depletion (Taylor and McLennan, 1985; Hofmann, 1997), a distinct enrichment of Rb, Ba, K, Th, La, and Ce (Jamali, 2017) along with the Sr-Nd isotopic composition (Jung, 1999) demonstrate the important role of crustal assimilation during the magmatic evolution of the Hamech intermediate intrusions unlike the mafic rocks.

To determine the source composition, the Sm/Yb vs. La/Sm (Figure 12a) and Gd/Yb vs. La/Yb (Figure 12b) diagrams were used (Shaw, 1970). These diagrams show that dioritic rocks originated from 1% to 3% partial melting of a spinel ± garnet lherzolite mantle while the mafic bodies originated from more than 8% partial melting of the depleted mantle with the spinel lherzolite composition. A low TiO_2 content and, consequently, high CaO/TiO_2 and Al_2O_3/TiO_2 ratios with possibly low Ti/V and Ti/Sc ratios confirm that mafic rocks originated from a depleted mantle (Crawford et al., 1989) with spinel combination (Temizel and Arslan, 2009).

Low $(Ce/Yb)_N$ ratios for intermediate intrusive rocks (4.87 to 7.07) and mafic bodies (0.52 to 0.78) indicate that parent magma originated from upper parts of the mantle,

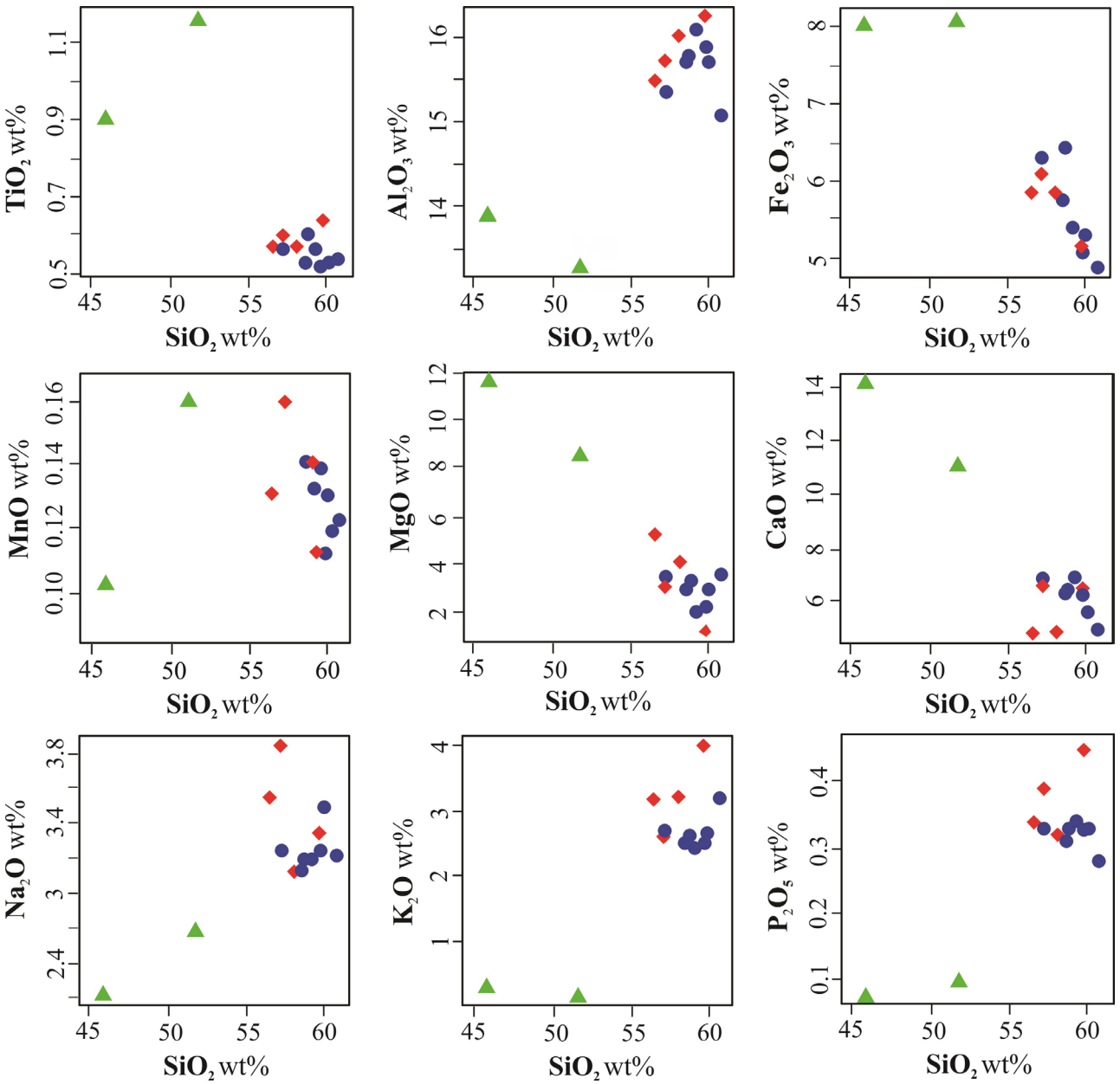

Figure 8. Plots of major elements vs. SiO_2 of the Hamech intrusive rocks.

low depths for intermediate intrusions (Cotton et al., 1995), and much shallower depths for mafic intrusives. The data from the Ce/Yb vs. Sm/Yb graph (Wang et al., 2002) confirm this motif very well (Figure 12c).

The Ce/Sm and Sm/Yb ratios (COBAN, 2007) in the Hamech intrusions vary from 8.85 to 10.33 and from 1.85 to 2.68 for dioritic rocks and from 2.44 to 3.17 and from 0.83 to 0.95 for gabbroic units, respectively. These ratios indicate that there is no garnet or it is rarely present as remaining mineral at the source of dioritic rocks (Figure 13a), which confirms previous information. According to La/Sm vs. Sm/Yb diagram (Kay and Mpodozis, 2001); pyroxene and amphibole existed at the source of dioritic rocks and pyroxene at the source of gabbroic rocks (Figure 13b). Clinopyroxene and amphiboles are stable at depths less than 35 km and 30 to 45 km, respectively (Kay and Mpodozis, 2001). Due to the lack of garnet at the source of gabbroic rocks, we suggest that their parent magma was formed at depths less than 50 km because garnet appears at depths greater than 45–50 km.

The Th/Yb vs. Ta/Yb diagram (Pearce, 1983) can be used to define magmatic source. According to this

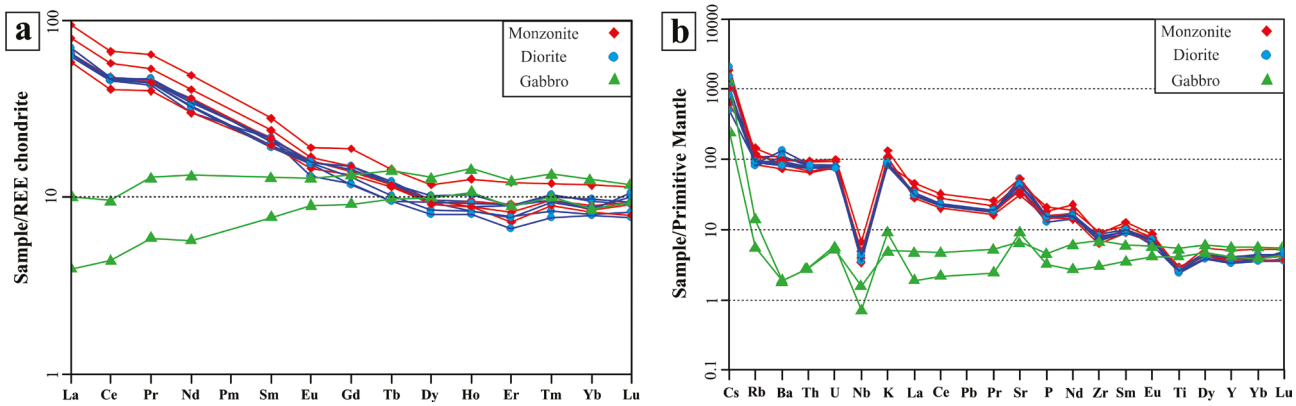

Figure 9. (a) Chondrite-normalized REE diagram for the Hamech intrusive rocks (Boynton, 1985). (b) Primitive Mantle-normalized REE diagram for the Hamech intrusive rocks (Sun and McDonough, 1989).

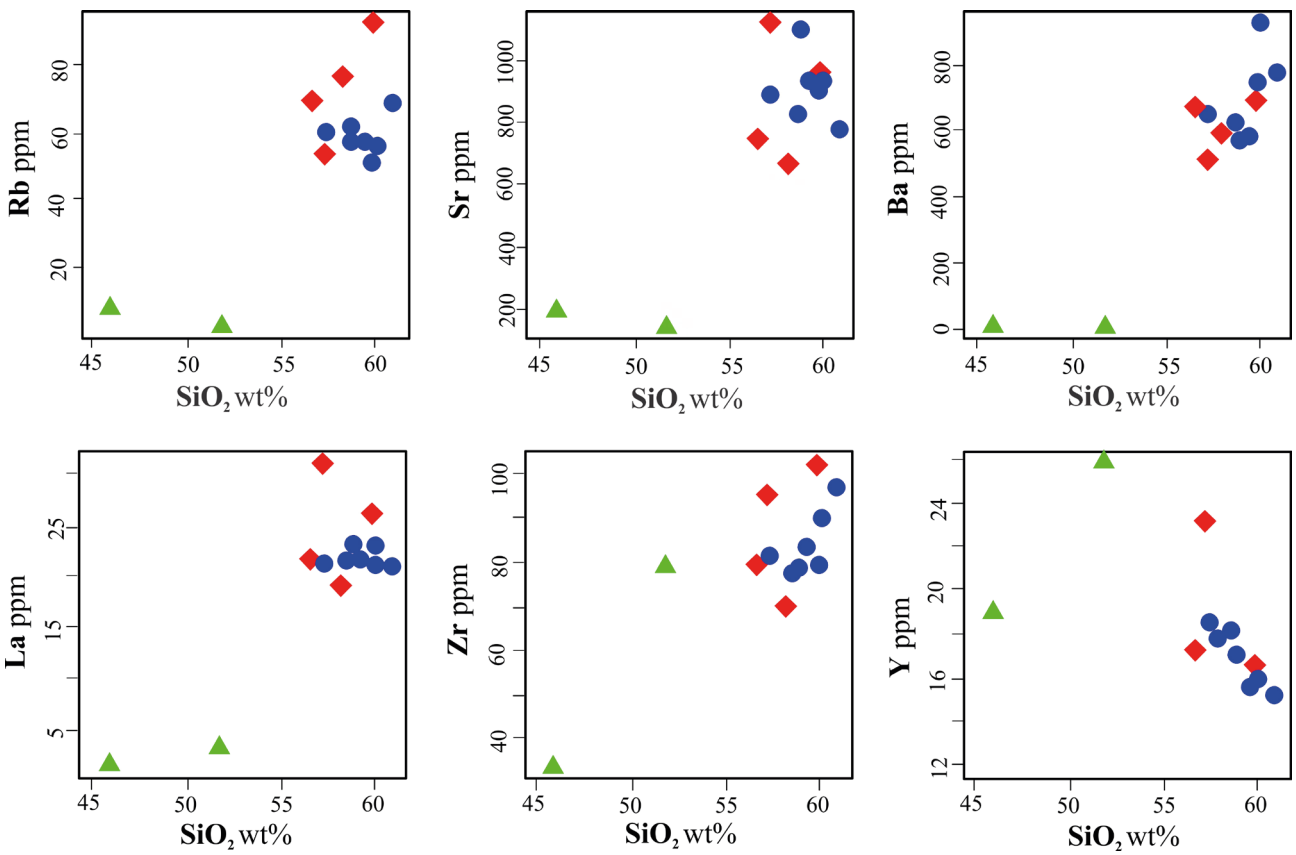

Figure 10. Plots of trace-element vs. SiO_2 of the Hamech intrusive rocks.

diagram (Figure 13c), dioritic rocks originated from enriched mantle and they are plotted parallel to the mantle metasomatism orientation. In Ba/La vs. Th/Nd diagram (Shaw, 1970), slab-derived fluids can be considered to be the main factor of metasomatism (Figure 13d) during dioritic rock formation.

5.1.2. Rb-Sr and Sm-Nd isotopic consequences

The similar initial Sr and Nd isotopic compositions in each of intermediate intrusions and gabbroic rocks separately suggest a considerable difference and consequently different characteristics in their origin. In addition, isotope characterization indicates that these rocks are epigenetic,

Table 4. The $^{87}Sr/^{86}Sr$ and $^{143}Nd/^{144}Nd$ isotopic ratios of the Hamech intrusive rocks.

Sample	Rock type	Rb (ppm)	Sr (ppm)	Sm (ppm)	Nd (ppm)	$^{87}Rb/^{86}Sr$	$^{87}/^{86}Sr$	$^{87}/^{86}Sr$ (i)	$^{147}Sm/^{144}Nd$	$^{143}/^{144}Nd$	eNd(0)	$^{143}/^{144}Nd(i)$	eNd(i)	TDM Ga
2.1E	Diorite	68.4	777.4	4.85	19.1	0.2545	0.704854	0.704716	0.1542	0.512672	0.66	0.512633	0.87	0.78
19E	Monzonite	92.3	959.6	4.85	25.6	0.2782	0.704961	0.704810	0.1150	0.512670	0.62	0.512641	1.02	0.77
50E	Monzonite	76.2	665.5	4.00	18.9	0.3312	0.704721	0.704541	0.1285	0.512723	1.66	0.512691	1.99	0.69
97E	Diorite	57.2	1109.3	3.98	20.7	0.1491	0.704961	0.704880	0.1168	0.512712	1.44	0.512683	1.83	0.70
73E	Gabbro	8.7	191.0	1.56	3.6	0.1317	0.704773	0.704704	0.2632	0.513077	8.56	0.513013	8.25	0.17
74E	Gabbro	3.6	143.1	2.65	6.4	0.0728	0.703437	0.703399	0.2515	0.513040	7.84	0.512979	7.58	0.23

The Sr-Nd isotopic composition of six whole-rock samples from the Hamech area. Errors are in 2σ. Initial $^{87}Sr/^{86}Sr$ and $^{143}Nd/^{144}Nd$ ratios were calculated using the crystallization age of 38.2 Ma for intrusive rocks including 2.1E (diorite), 19E (monzonite), 50E (monzonite), 97E (diorite), and 36.9 Ma for gabbroic rocks, i.e. 73E (gabbro) and 74E (gabbro), respectively. The CHUR value (Chondritic Uniform Reservoir) to determine the initial isotopic compositions of studied rocks taken from DePaolo, 1988.

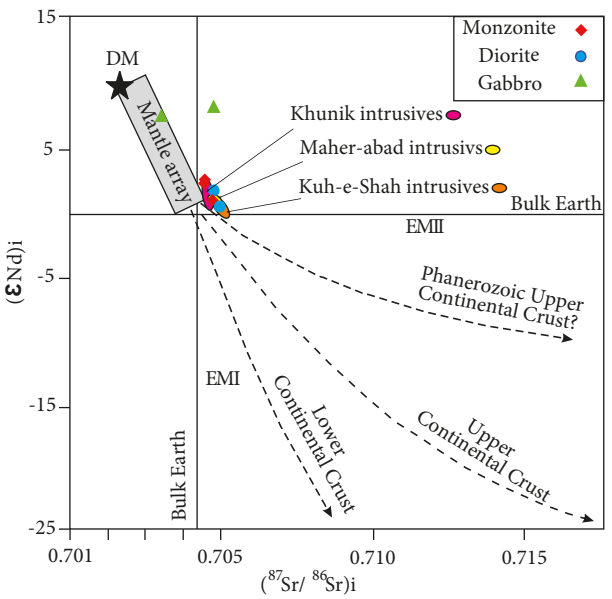

Figure 11. ƐNd(i) vs. ($^{87}Sr/^{86}Sr$)i diagram for the Hamech intrusive rocks. Reference data sources: upper continental crust (Taylor and McLennan, 1985); lower continental crust (Rollinson, 1993; Rudnick, 1995) with those of MORB (Sun and McDonough, 1989; Rollinson, 1993), DM (McCulloch and Bennett, 1994), OIB (Vervoort et al., 1999), IAB (Arjmandzadeh and Santos, 2014), and mantle array (Gill, 1981; Wilson, 1989; McCulloch et al., 1994). DM, Depleted Mantle; EM I and EM II, enriched mantle sources.

being derived from the different parental magmas by magmatic differentiation processes. The recorded small variation of isotopic ratios in the same groups, in the intermediate intrusions, can be attributed to either the varying crustal assimilation (but always in small degrees) or heterogeneity in the magma source (Nabatian et al., 2014). As mentioned by Arjmandzadeh et al. (2011) and Menzies et al. (1993), the hydrothermal alteration may also cause some displacement of their isotope composition and consequently higher $^{87}Sr/^{86}Sr$ ratio. The fact that mobility rate of Sr relative to the REEs is more than five times higher during the postmagmatic hydrothermal alteration was presented by researchers such as Anderade et al. (1999). Moreover, microscopic evidence and alteration in one of the gabbro samples are confirmed by the higher amount of $^{87}Sr/^{86}Sr$ ratio.

The $^{87}Sr/^{86}Sr(i)$ and $^{143}Nd/^{144}Nd(i)$ vs. MgO graphs (Figures 14a and 14b) exhibit approximately horizontal trends for the intermediate samples. Both diagrams reveal role of fractional crystallization in the evolution of intrusives.

According to Chappell and White (1974), the values of ($^{87}Sr/^{86}Sr$)i lower than 0.708 (between 0.704 and 0.706) are representative of I-type granitoids. Therefore, the obtained values provide further evidence in favor of the I-type nature of the studied granitoids (Hamech intrusion bodies).

5.2. Fractionation and assimilation

The primary cause of change in the composition of magma is cooling, which causes the magma to begin to crystallize minerals from the melt or liquid portion of the magma (Fractional crystallization; FC). Contamination is another cause of magma differentiation. Contamination can be caused by assimilation of wall rocks (assimilation), mixing of two or more magmas or even by replenishment of the magma chamber with fresh, hot magma (mixing). These three processes cause the most effective changes in the composition of the magma that will be produced.

In this section, we are trying to use trace element constraints on the relationship between two groups of rocks in the study area, i.e. gabbros and diorites. The unusual association of gabbroic units with intermediate intrusive rocks in the Hamech area raises the question of the importance of fractionation vs. assimilation and

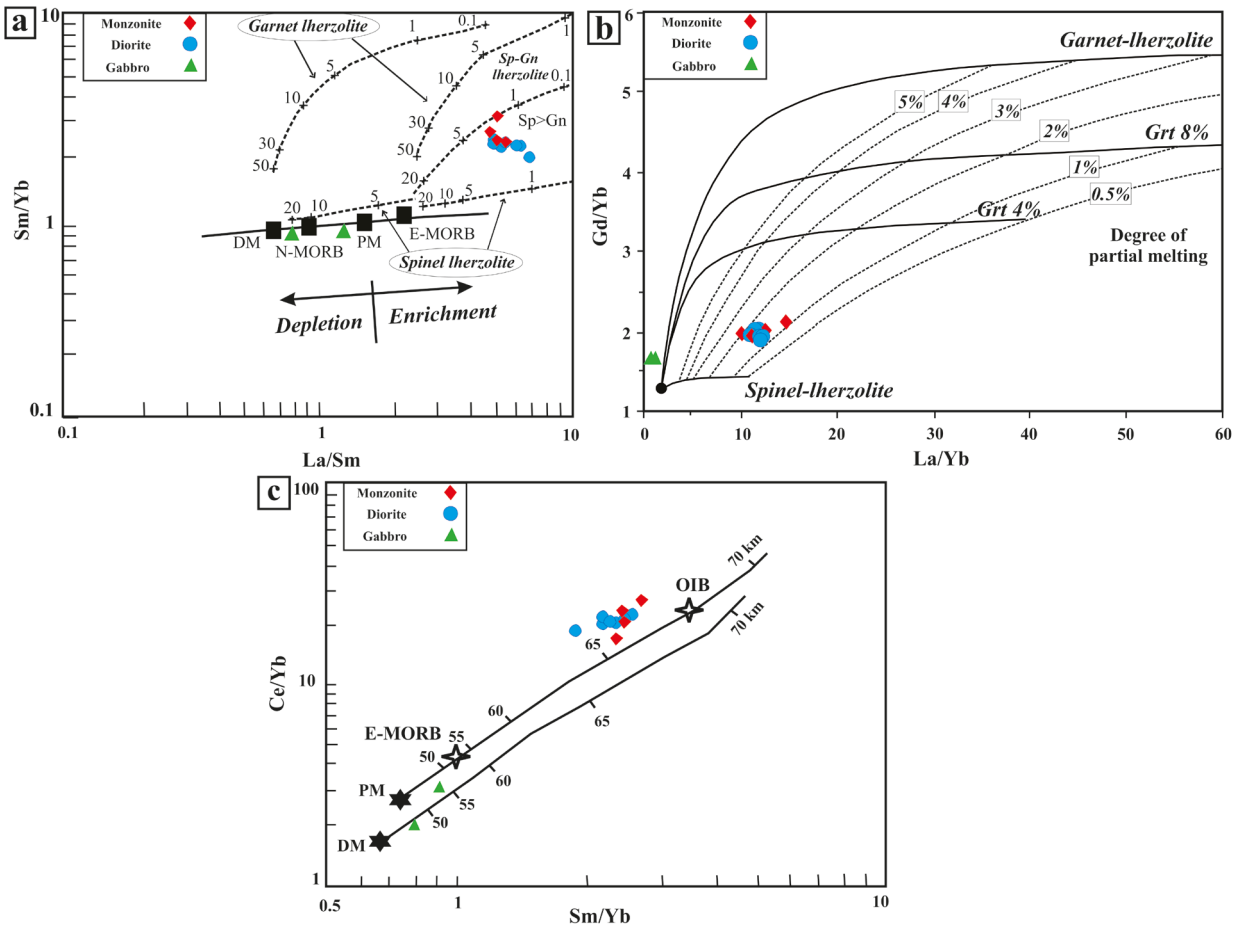

Figure 12. (a) Sm/Yb vs. La/Sm diagram (Shaw, 1970), (b) Gd/Yb vs. La/Yb diagram. Accumulated fractional melting is assumed and partition coefficients reported in Halliday et al. (1995) are used in the calculation. (c) Ce/Yb vs. Sm/Yb diagram (Wang et al., 2002) for Hamech intrusive rocks.

mixing processes in the evolution of the intrusive rocks.

For this purpose, Hamech intrusive rocks plotted in the La vs. Nb and V/Co vs. La/Sm diagrams (Figures 15a and 15b). These diagrams show examples from the evolution of calculated trace element ratios for models of: (1) fractional crystallization (FC); (2) assimilation fractional crystallization (AFC); and (3) a binary mixing model. The observed trends appear to be consistent with an evolution of the dioritic rocks by AFC process from a magma of different composition to the gabbroic rocks. This model is consistent with the observed trends and could also account for the discrete trace element patterns. Gabbroic rocks show more compatibility with FC trend. However, the mafic samples plot near the source that shows low degree of fractional crystallization from a different magma of the dioritic rocks (Figure 15).

5.3. Tectonic setting

In order to determine the tectonic setting of the Hamech intrusive rocks, Rb vs. Ta + Yb (Figure 16a) and Ta vs. Yb diagrams (Figure 16b) by Pearce et al. (1984) were used. The studied rocks plot largely in the fields of volcanic arc granitoids (VAG). Also, in the La/Yb vs. Th/Yb (Condie, 1989) and Rb/Zr vs. Nb (Brown et al., 1984) diagrams, the Hamech intrusive rocks fall into the field of continental margin arc (Figures 16c, 16d) and into the low maturity arc field (Figure 16d). Most of the Eocene magmatic rocks of Iran show these features, probably due to the low thickness of crust at this time (please see Richards et al., 2012; Jamali, 2017).

5.4. Geodynamic implications

The eastern part of Iran had a complex tectonic history related to the evolution of Sistan Ocean, with its remnant known as the Flysch Zone between Lut and Helmand Blocks. This ocean probably was opened by the Early Cretaceous (Babazadeh and de Wever, 2004) and its generation has been in progress during Middle Cretaceous (Zarrinkoub et al., 2012). The mechanism and final closure time of the Sistan Ocean (Middle Eocene

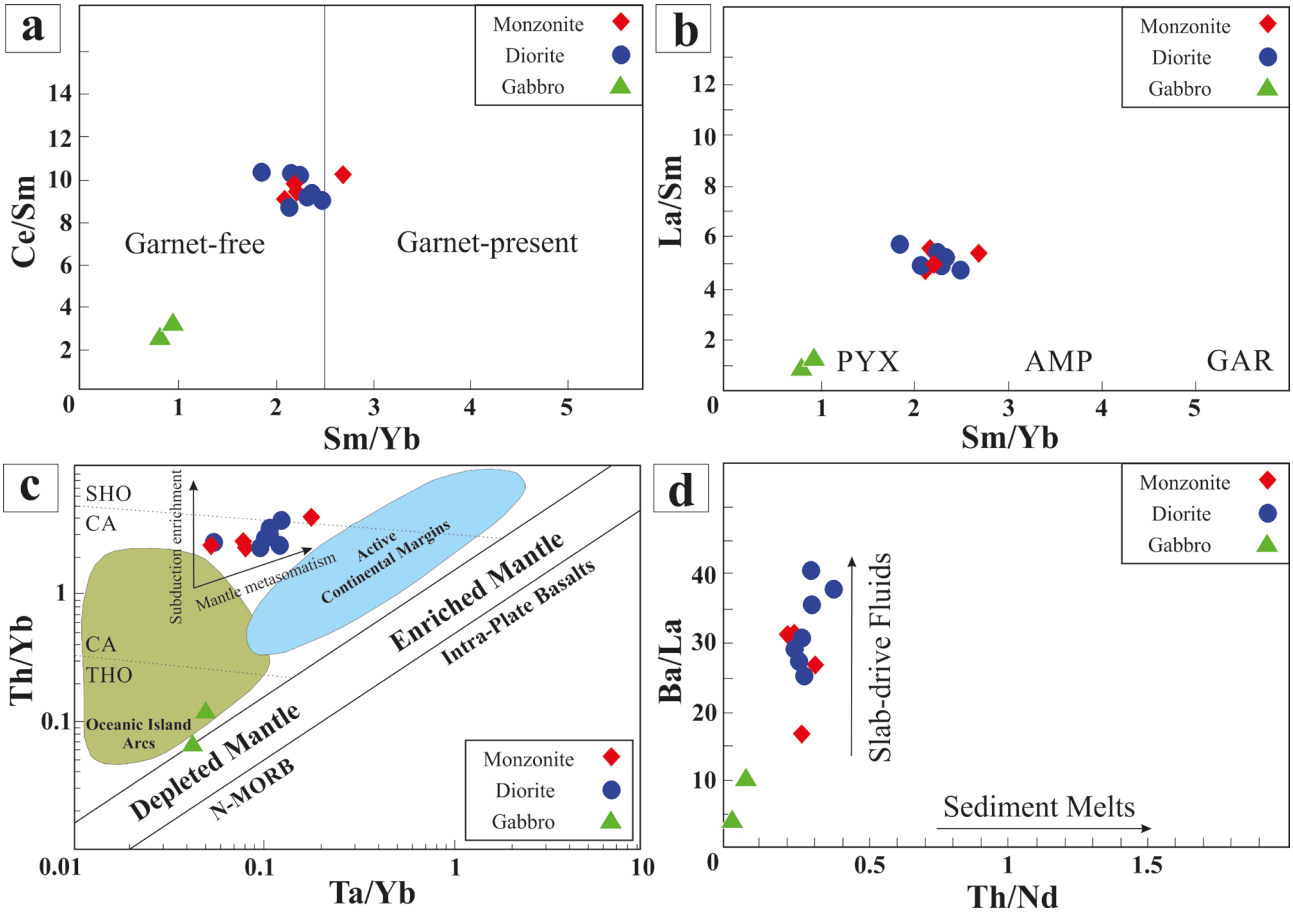

Figure 13. (a) Ce/Sm vs. Sm/Yb diagram (COBAN, 2007) showing the absence of garnet at source, (b) La/Sm vs. Sm/Yb plot showing the fields for the Hamech intrusive rocks, PYX = pyroxene, AMP = amphobole, GAR = garnet: garnet (modified from Kay and Mpodozis, 2001), (c) Th/Yb vs. Ta/Yb diagram (Pearce, 1983) for the Hamech intrusive rocks (d). Ba/La vs. Th/Nd diagram (Shaw, 1970) that indicates all the samples follow the slab-derived fluid melt array.

or Late Cretaceous) remain poorly understood. Various models of evolution are presented for this ocean, involving extensional tectonic setting (Jung et al., 1983; Tarkian et al., 1983; Samani and Ashtari, 1992) along with other subduction theories like eastward subduction beneath the Afghan Block (Camp and Griffis, 1982; Tirrul et al., 1983), western subduction beneath the Lut Block (Zarrinkoub et al., 2012), eastward intraoceanic subduction (Saccani et al., 2010), and two-sided subduction (Arjmandzadeh et al., 2011), and northeastward subduction beneath the north-central Lut Block (Saadat and Stern, 2016) have been put forward in this regard.

Although most of the processes and developments in tectonics, magmatism, and metallogeny are justifiable by two-sided asymmetric subduction hypothesis, as mentioned by Karimpour et al. (2007), abundant intrusive bodies in the Lut Block might be formed under different tectonic conditions that should be considered. According to the fact that two-sided subduction is not common in subduction zones, the age of intrusive rocks decreases from the north to the south of the Lut Block (from 43.3 Ma. in Kaybar Kuh to 33.3 Ma. in Chah-Shaljami; Figure 1). Moreover, considering the parallel repeated exposure of ophiolitic outcrops (Figure 1; black color) in the NW–SE direction in the NW part of the Flysch Zone, we suggest that Sistan Ocean had branches at its northern end, and its closure starts from the north without emphasis on subduction under the Afghan Block. Subduction under the Lut Block caused extensive magmatism at Tertiary (Eocene to Oligocene) window of eastern Iran. This hypothesis (Figure 17) is in line with those confirm subduction under the Lut Block.

6. Conclusions

The exposed intrusions in the Hamech area are mainly composed of two groups including intermediate rocks (dioritic to monzonitic rocks; 38.2 ± 1 Ma-Bartonian) and mafic bodies (gabbroic rocks; 36.9 ± 1 Ma-Priabonian)

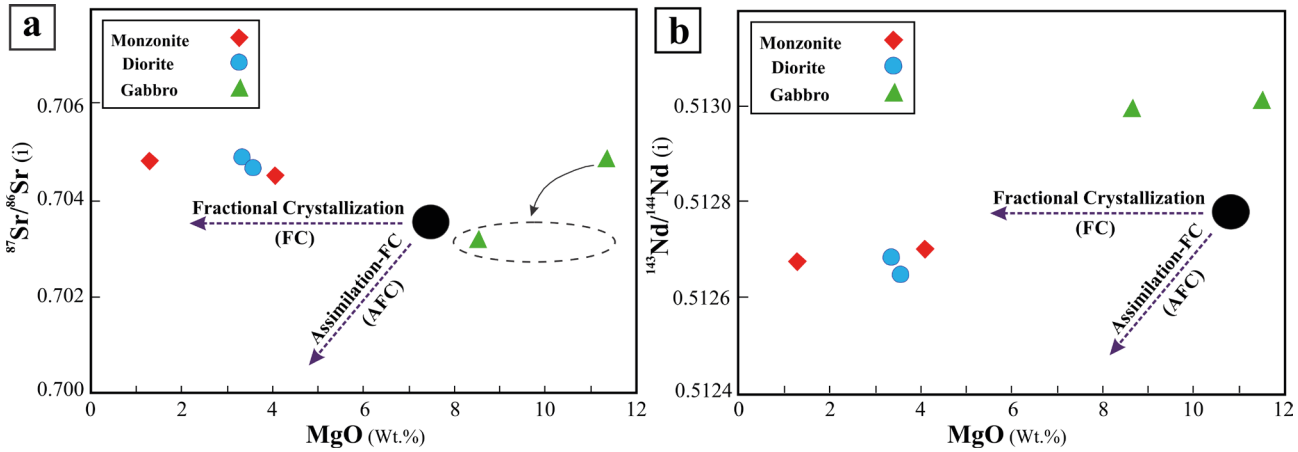

Figure 14. Diagrams of MgO vs. $^{87}Sr/^{86}Sr$(i) and $^{143}Nd/^{144}Nd$(i) for the Hamech intrusive rocks. (a) The variation of MgO vs. $^{87}Sr/^{86}Sr$(i) diagram, (b) MgO vs.$^{143}Nd/^{144}Nd$(i) diagram.

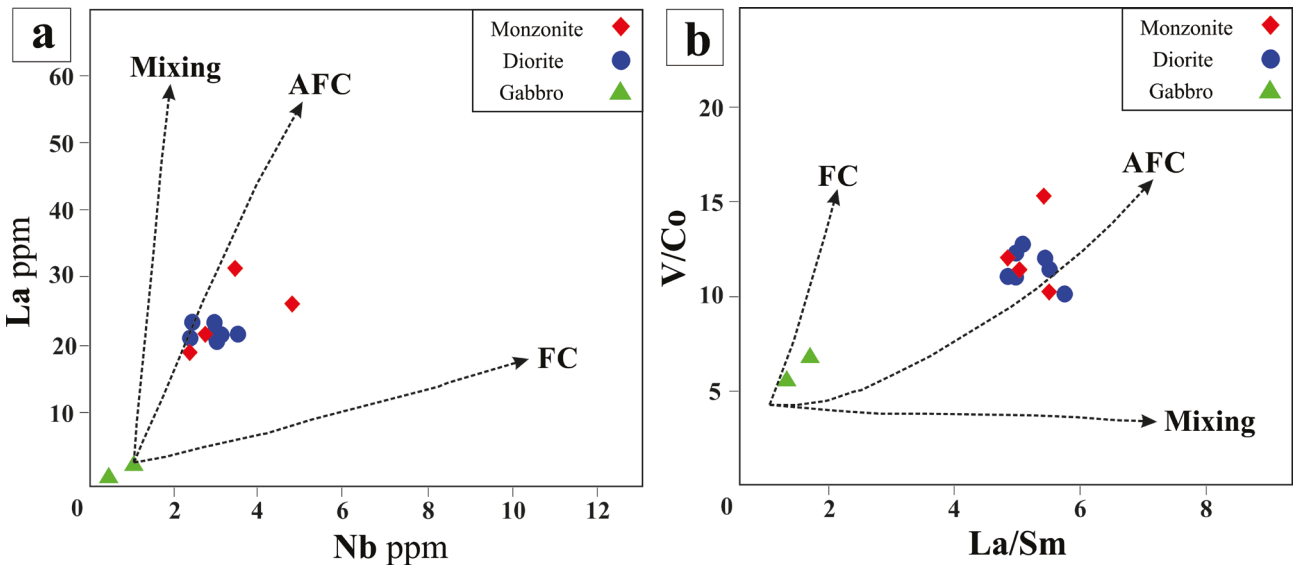

Figure 15. Modeling of fractional crystallization (FC), assimilation-fractional crystallization (AFC) and mixing for the Hamech intrusive rocks in La vs. Nb, (a) and V/Co vs. La/Sm, (b) diagrams.

that intruded into a little older volcanic rock (andesite to dacite; 38.6 ± 1 Ma-Bartonian). These intrusions are metaluminous, I-type high-K calc-alkaline tholeiitic composition.

Geochemical data demonstrate that parent magmas of the Hamech intrusions originated from partial melting of an enriched mantle with spinel ± garnet lherzolite for dioritic rocks and from depleted mantle with spinel-lherzolite composition for gabbroic rocks. Whole-rock geochemistry as well as isotope characteristics show that intrusive rocks in the Hamech area cannot have been derived from the same magma. The parallel trend of REEs pattern in dioritic and gabbroic rocks suggests a similarity of magmatic processes during the formation, separately. Meanwhile, dioritic rocks display similar averaged values of trace elements higher than those of gabbroic types. Also, difference in their REEs enrichment pattern, suggests their different origin and/or magmatic process during the evolution. The LREE/HREE enrichment in dioritic rocks is an indicator of crustal contamination or melts created in subduction zones by low degrees of partial melting.

The similar initial Sr and Nd isotopic compositions in each of intermediate intrusions and gabbroic rocks separately, suggest a considerable difference and consequently different characteristics in their origin (at least two parental magmas). The positive values of

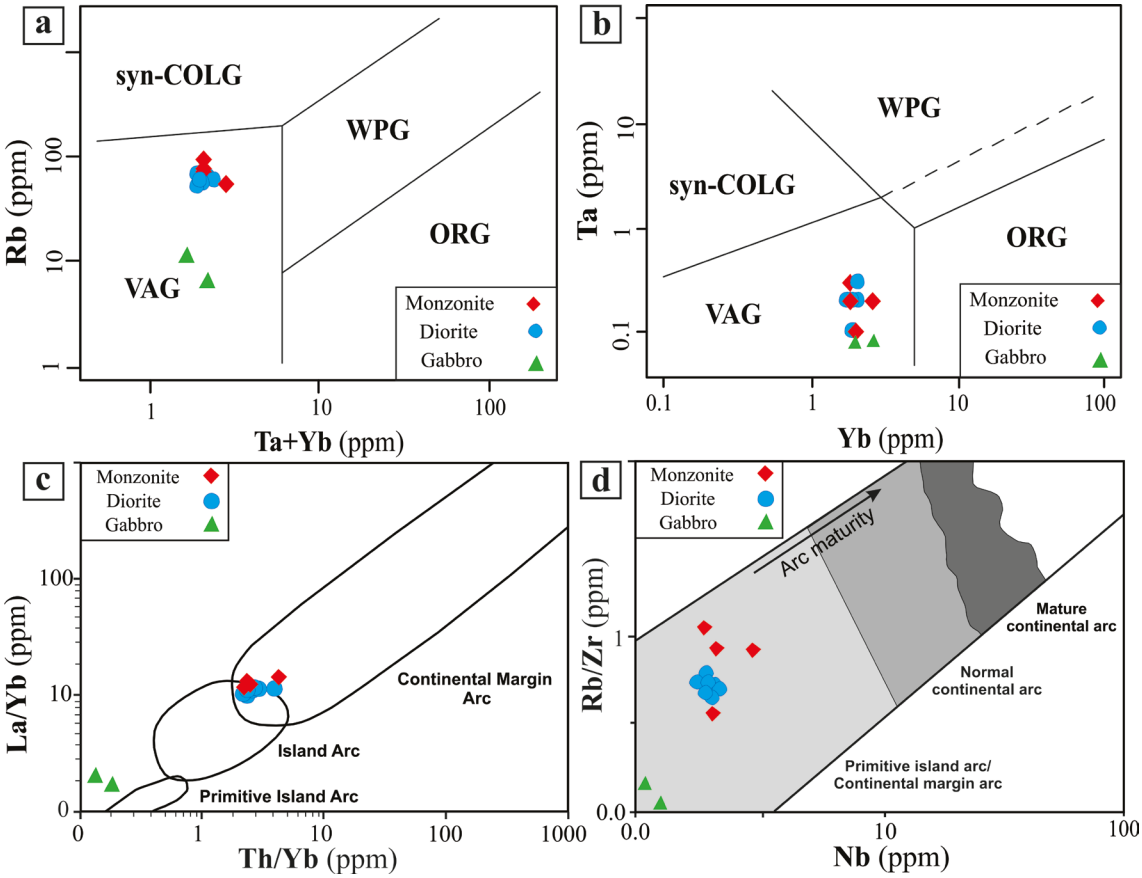

Figure 16. (a) and (b)Tectonic discrimination plots (Pearce et al., 1984) for Hamech intrusive rocks, (c) La/Yb vs. Th/Yb diagram (after Condie, 1989) (d) Rb/Zr vs. Nb diagram of the Hamech intrusive rocks (Brown et al., 1984).

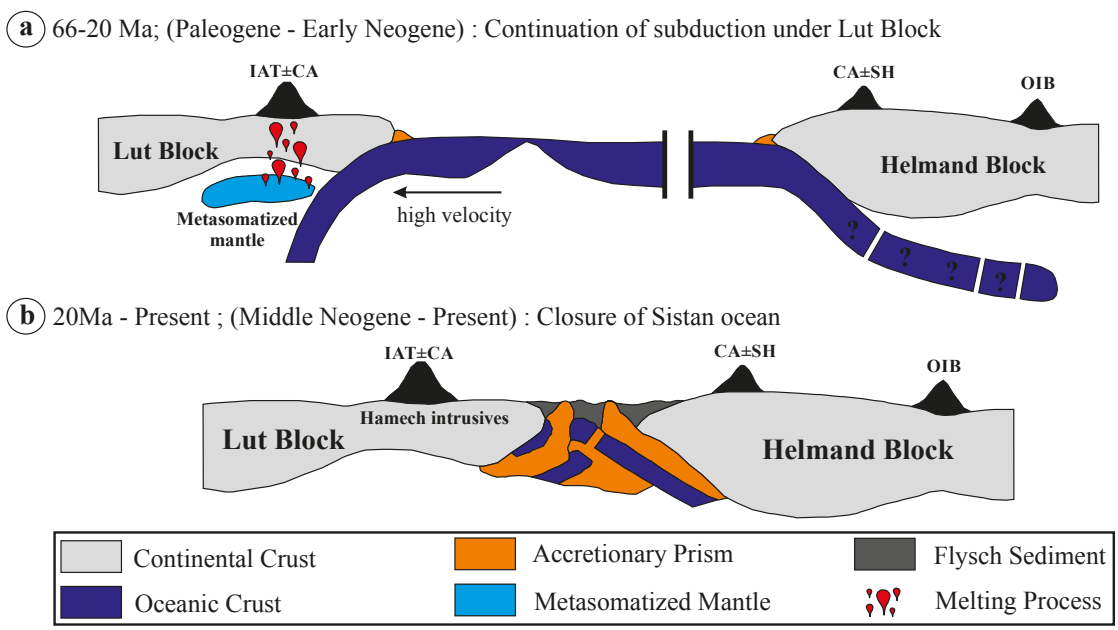

Figure 17. Simplified geodynamic model is presented as a hypothesis for the tectono-magmatic and metallogenic setting of the eastern part of the Lut Block, especially Kuh-e-Shah region, during Eocene.

ƐNd(i) for gabbroic rocks reveal lithospheric mantle-derived melts but lower values for intermediate rocks suggest contribution of crustal melts. Based on whole-rock geochemical features as well as isotope characteristics, they cannot have been derived from same magma. Trace element geochemistry confirms evolution of dioritic rocks by AFC process from magmas of different composition to the gabbroic rocks. This model is consistent with the observed trends in REE patterns. However, gabbroic rocks show more compatibility with FC trend.

All data suggest that the Hamech intrusions have been derived from mantle and crustal end members but the mantle component seems to be enriched due to previous subduction in a low maturity continental margin arc setting related to the convergence of the Afghan and Lut Blocks during subduction of Sistan oceanic crust at the Eocene.

Acknowledgments

This study is a part of the first author's PhD thesis carried out under the supervision of the second and third authors and has been supported by the Research Foundation of Ferdowsi University of Mashhad, Iran (Project No. 3.36963). The authors wish to thank the Ministry of Sciences, Research, and Technology of Iran for financial support during the sabbatical research of the first author in Portugal. The authors gratefully acknowledge the editor in Chief Prof. Dr. Orhan TATAR and constructive comments on the paper offered by the Assoc. Prof. Dr. Namık AYSAL, Prof. Dr. Mehmet ARSLAN, and other anonymous referees.

References

Abdi M, Karimpour MH (2013). Petrochemical characteristics and timing of Middle Eocene granitic magmatism in Kooh-Shah, Lute Block, Eastern Iran. Acta Geol Sin 84: 1032-1044.

Aghanabati A (1998). Major sedimentary and structural units of Iran (map). J Geosci 7: 29-30.

Aghanabati A (2005). Geology of Iran: Geological Survey of Iran, Tehran, Iran (in Persian).

Alavi M (1991). Sedimentary and structural characteristics of the Paleo-Tethys remnants in northeastern Iran. Geol Soc Am Bull 103: 983-992.

Andrade FRD, Möller P, Höhndorf A (1999). The effect of hydrothermal alteration on the Sr and Nd isotopic signatures of the Barra do Itapirapuã carbonatite, southern Brazil. The J Geol 107: 177-191.

Arjmandzadeh R (2011). Mineralization, geochemistry, geochronology, and determination of tectonomagmatic setting of intrusive rocks in Dehsalm and Chahshaljami prospect areas, Lut block, east of Iran. PhD, Ferdowsi University of Mashhad, Mashhad, Iran.

Arjmandzadeh R, Karimpour MH, Mazaheri SA, Santos JF, Medina JM, Homam SM (2011). Sr–Nd isotope geochemistry and petrogenesis of the Chah-Shaljami granitoids (Lut Block, eastern Iran). J Asian Earth Sci 41: 283-296.

Arjmandzadeh R, Santos JF (2014). Sr–Nd isotope geochemistry and tectonomagmatic setting of the Dehsalm Cu–Mo porphyry mineralizing intrusives from Lut Block, eastern Iran. Int J Earth Sci 103: 123-140.

Asiabanha A, Bardintzeff JM, Kananian A, Rahimi G (2012). Post-Eocene volcanics of the Abazar district, Qazvin, Iran: Mineralogical and geochemical evidence for a complex magmatic evolution. J Asian Earth Sci 45: 79-94.

Babazadeh SA, De Wever P (2004). Radiolarian Cretaceous age of Soulabest radiolarites in ophiolite suite of eastern Iran. B Soc géol Fr 175: 121-129.

Berberian M (1981). Towards a paleogeography and tectonic evaluation of Iran. Can J Earth Sci 18: 210-265.

Berberian M, Jackson JA, Qorashi M, Khatib MM, Priestley K, Talebien M, Ghafuri-Ashtiani M, (1999). The 1997 May 10 Zirkuh (Qaenat) earthquake (M.W 7.2): aulting along the Sistan suture zone of eastern Iran. Geophys J Int 136: 671-694.

Beydokhti RM, Karimpour MH, Mazaheri SA, Santos JF, Klötzli U (2015). U–Pb zircon geochronology, Sr–Nd geochemistry, petrogenesis and tectonic setting of Mahoor granitoid rocks (Lut Block, Eastern Iran). J Asian Earth Sci 111: 192-205.

Blein O, Lapierre H, Schweickert RA (2001). A Permian island-arc with a continental basement: the Black Dyke Formation Nevada, North American Cordillera. Chem Geol 175: 543-566.

Boynton WV (1984). Cosmochemistry of the rare earth elements: meteorite studies. In: Henderson P, editor. Rare Earth Element Geochemistry. Amsterdam, the Netherlands: Elsevier, pp. 63-107.

Brown GC, Thorpe RS, Webb PC (1984). The geochemical characteristics of granitoids in contrasting arcs and comments on magma sources. J Geol Soc 141: 413-426.

Camp V, Griffis R (1982). Character, genesis and tectonic setting of igneous rocks in the Sistan suture zone, eastern Iran. Lithos 15: 221-239.

Chang Z, Vervoort JD, McClelland WC, Knaak C (2006). U-Pb dating of zircon by LA-ICP-MS. Geochem Geophy Geosy 7: 1-14.

Chappell BJ, White AJR (1974). Two contrasting granite types. Pac Geol 8: 173-174.

Condie KC (1989). Geochemical changes in basalts and andesites across the Archean-Proterozoic boundary: identification and significance. Lithos 23: 1-18.

Cotton J, Le Dez A, Bau M, Caroff M, Maury RC, Dulski P, Fourcade S, Bohn M, Brousse R (1995). Origin of anomalous rare-earth element and yttrium enrichments in subaerially exposed basalts, evidence from French Polynesia. Chem Geol 119: 115-138.

Crawford AJ, Falloon TJ, Green DH (1989). Classification, petrogenesis and tectonic setting of boninites. In: Crawford AJ, editor. Boninites and Related Rocks, London, UK: Unwin Hyman, pp. 1-49.

Çoban H (2007). Basalt magma genesis and fractionation in collision- and extension-related provinces: a comparison between eastern, central western Anatolia. Earth Sci Rev 80: 219-238.

Defant MJ, Drummond MS (1990). Derivation of some modern arc magmas by melting of young subduction lithosphere. Nature 347: 662-665.

Depaolo DJ (1988). Neodymium Isotope Geochemistry. Berlin, Germany: Springer.

Drake MJ, Weill DF (1975). Partition of Sr, Ba, Ca, Y, Eu^{2+}, Eu^{3+} and other REE between plagioclase feldspar and magmatic liquid: an experimental study. Geochim Cosmochim Act 39: 689-712.

Eftekharnejad J (1980). separating different parts of Iran in vies of constructional position related too sedimentary basins, Petrol Association Publication 82.

Fan WM, Guo F, Wang YJ, Zhang M (2004). Late Mesozoic volcanism in the northern Huaiyang tectono-magmatic belt, central China: partial melts from a lithospheric mantle with subducted continental crust relicts beneath the Dabie orogen? Chem Geol 209: 27-48.

Frey FA, Chappell BW, Roy SD (1978). Fractionation of rare-earth elements in the Tuolumne Intrusive Series, Sierra Nevada batholith, California. Geology 6: 239-242.

Ghorbani M (2013). The Economic Geology of Iran: Mineral Deposits and Natural Resources. 1st ed. Dordrecht, the Netherlands: Springer Science and Business Media.

Gill JB (1981). Orogenic Andesites and Plate Tectonics, Mineral and Rocks 6. Berlin, Germany: Springer-Verlag.

Halliday AN, Lee DC, Tommasini S, Davies GR, Paslick CR, Fitton JG, James DE (1995). Incompatible trace elements in OIB and MORB and source enrichment in the sub-oceanic mantle. Earth Planet Sc Lett 133: 379-395.

Hanson GN (1980). Rare earth elements in petrogenetic studies of igneous systems. Annu Rev Earth Pl Sc 8: 371-406.

Helvacı C, Ersoy EY, Sözbilir H, Erkül F, Sümer Ö, Uzel B (2009). Geochemistry and $^{40}Ar/^{39}Ar$ geochronology of Miocene volcanic rocks from the Karaburun Peninsula: implications for amphibolebearing lithospheric mantle source, Western Anatolia. J Volcanol Geoth Res 185: 181-202.

Hofmann AM (1997). Mantle geochemistry: the message from oceanic volcanism. Nature 385: 219-229.

Hosseinkhani A, Karimpour MH, Shafaroudi AM, Santos JF (2017). U-Pb geochronology and petrogenesis of intrusive rocks: Constraints on the mode of genesis and timing of Cu mineralization in SWSK area, Lut Block. J Geochem Explor 177: 11-27.

Jamali H (2017). The behavior of rare-earth elements, zirconium and hafnium during magma evolution and their application in determining mineralized magmatic suites in subduction zones: constraints from the Cenozoic belts of Iran. Ore Geol Rev 81: 270-279.

Jung D, Keller J, Khorasani R, Marcks C, Baumann A, Horn P (1983). Petrology of the Tertiary magmatic activity the northern Lut area, East of Iran. Ministry of Mines and Metals, GSI, Geodynamic Project (geotraverse) in Iran, No. 51, pp. 285-336.

Jung S (1999). The role of crustal contamination during the evolution of continental rift-related basalts: a case study from the Vogelsberg area (central Germany). Geolines 9: 48-58.

Karimpour MH, Malekzadeh Shafaroudi A, Mazaheri SA, Haidarian Shahri MH (2007). Magmatism and different types of mineralization in Lut Block. In: 15th Symposium of Iranian Society of Crystallography and Mineralogy, Ferdowsi University of Mashhad, Iran, pp. 598-604.

Karimpour MH, Stem CR, Farmer L, Saadat S, Malekezadeh A (2011). Review of age, Rb-Sr geochemistry and petrogenesis of Jurassic to Quaternary igneous rocks in Lut Block, Eastern Iran. Geopersia 1: 19-36.

Kay SM, Mpodozis C (2001). Central Andean ore deposits linked to evolving shallow subduction system and thickening crust. GSA today 11: 4-9.

Ludwig KR (2007). Isoplot version 3.7, User's Manual. Berkeley Geochronology Center, Special Publication 4.

Mahdavi A, Karimpour MH, Mao J, Shahri MRH, Shafaroudi AM, Li H (2016). Zircon U–Pb geochronology, Hf isotopes and geochemistry of intrusive rocks in the Gazu copper deposit, Iran: petrogenesis and geological implications. Ore Geol Rev 72: 818-837.

Malekzadeh Shafaroudi A (2009). Geology, mineralization, alteration, geochemistry, Microthermometry, radioisotope and Petrogenesis of intrusive rocks copper-gold porphyry Maherabad and Khopik. PhD, Ferdowsi University of Mashhad, Mashhad, Iran.

Malekzadeh Shafaroudi A, Karimpour MH, Stern CR (2015). The Khopik porphyry copper prospect, Lut Block, Eastern Iran: geology, alteration and mineralization, fluid inclusion, and oxygen isotope studies. Ore Geol Rev 65: 522–544.

Martin H (1987). Petrogenesis of Archaean trondhjemites, tonalites, and granodiorites from eastern Finland: major and trace element geochemistry. J Petrol 28: 921-953.

McCulloch MT, Bennett VC (1994). Progressive growth of the Earth's continental crust and depleted mantle: geochemical constraints. Geochim Cosmochim Act 58: 4717-4738.

Menzies MA, Long A, Ingeram G, Talnfi M, Janfcky D (1993). MORB preidotite–seawater interaction: experimental constrains on the behavior of trace elements. $^{87}Sr/^{86}Sr$ and $^{143}Nd/^{144}Nd$ ratios. In: Princhard HM, Alabaster T, Harris NBW, Neary CR, editors. Magmatic Process and Plate Tectonics, Geological Society, London, Special Publications, vol. 76, pp. 309-322.

Middlemost EAK (1985). Magmas and Magmatic Rocks. London, UK: Longman.

Nabatian G, Ghaderi M, Neubauer F, Honarmand M, Liu X, Dong Y, Jiang S, Quadt A, Bernroide M (2014). Petrogenesis of Tarom high-potassic granitoids in the Alborz-Azarbaijan belt, Iran: geochemical, U–Pb zircon and Sr–Nd–Pb isotopic constraints. Lithos 184: 324-345.

Nicholson KN, Black PM, Hoskin PWO, Smith IEM (2004). Silicic volcanism and back-arc extension related to migration of the Late Cainozoic Australian- Pacific plate boundary. J Volcanol Geoth Res 131: 295-306.

Pearce JA (1983). Role of the sub-continental lithosphere in magma genesis at active continental margins. In: Hawkesworth CJ, Norry MJ, editors. Continental Basalts and Mantle Xenoliths. Nantwich, UK: Shiva Publisher, pp. 230-249.

Pearce JA, Harris NB, Tindle AG (1984). Trace element discrimination diagrams for the tectonic interpretation of granitic rocks. J petrol 25: 956-983.

Peccerillo A, Taylor SR (1976). Geochemistry of Eocene calc-alkaline volcanic rocks from the Kastamonu area (northern Turkey). Contrib Mineral Petr 58: 63-81.

Richards JP, Spell T, Rameh E, Razique A, Fletcher T (2012). High Sr/Y magmas reflect arc maturity, high magmatic water content, and porphyry Cu±Mo±Au potential: examples from the Tethyan arcs of central and eastern Iran and western Pakistan. Econ Geol 107: 295-332.

Rollinson HR (1993). Using Geochemical Data: Evaluation, Presentation, Interpretation. Essex, UK: Longman Science and Technical.

Rollinson H (2014). Plagiogranites from the mantle section of the Oman Ophiolite: models for early crustal evolution. Geological Society, London, Special Publications 392: 247-261.

Rudnick RL (1995). Making continental crust. Nature 378: 571-578.

Saadat S, Stern CR (2016). Distribution and geochemical variations among paleogene volcanic rocks from the north-central Lut block, eastern Iran. Iran J Earth Sci 8: 1-24.

Saccani E, Delavari M, Beccaluva L, Amini SA (2010). Petrological and geochemical constraints on the origin of the Nehbandan ophiolitic complex (eastern Iran): implication for the evolution of the Sistan Ocean. Lithos 117: 209-228.

Salati E, Karimpour MH, Malekzadeh Shafaroudi A, Heydarian Shahri MR, Farmer L, Stern Ch (2012). Zircon U–Pb geochronology, Sr–Nd isotope geochemistry, and petrogenetic study of Kaybar kuh oxidan granitoids (Sout-West of Khaf). J Econ Geol 4: 285-301 (in Persian).

Samani B, Ashtari S (1992). Geological evolution of Sistan and Baluchestan area. Geological Survey of Iran, J earth sci 4: 72-85 (in Persian with English abstract).

Samiee S, Karimpour MH, Ghaderi M, Haidarian Shahri MR, Kloetzli O, Santos JF (2016). Petrogenesis of subvolcanic rocks from the Khunik prospecting area, south of Birjand, Iran: Geochemical, Sr–Nd isotopic and U–Pb zircon constraints. J Asian Earth Sci 115: 170-182.

Shand SJ (1949). Eruptive Rocks: Their Genesis, Composition, Classification, and Their Relation to Ore-deposits. Thomas Murby.

Shaw DM (1970). Trace element fractionation during anataxis. Geochim Cosmochim Act 34: 237-243.

Stöcklin J, Eftekhar-Nezhad J, Hushmand-Zadeh A (1965). Geology of the Shotori range (Tabas area, east Iran) (No. 3), Geological Survey of Iran.

Stocklin J (1968). Structural history and tectonics of Iran: a review. AAPG Bull 52: 1229-1258.

Stocklin J, Nabavi MH (1973). Tectonic map of Iran. Geological Survey of Iran.

Sun SS, McDonough WF (1989). Chemical and isotopic systematics of oceanic basalts: implications for mantle composition and processes. Geol Soc Sp 42: 313-345.

Tarkian M, Lotfi M, Baumann A (1983). Tectonic, magmatism and the formation of mineral deposits in the central Lut, east Iran. Ministry of mines and metals, GSI, geodynamic project (geotraverse) in Iran, 51: 357-383.

Taylor SR, McLennan SM (1985). The Continental Crust: Its Composition and Evolution. Oxford, UK: Blackwell.

Temizel I, Arslan M (2009). Mineral chemistry and petrochemistry of post-collisional Tertiary mafic to felsic cogenetic volcanics in the Ulubey (Ordu) area, Eastern Pontides, NE Turkey. Turk J Earth Sci 18: 29-53.

Thirlwall MF, Smith TE, Graham AM, Theodorou N, Hollings P, Davidson JP, Arculus RJ (1994). High field strength element anomalies in arc lavas: source or process? J Petrol 35: 819-838.

Tirrul R, Bell IR, Griffis RJ, Camp VE (1983). The Sistan suture zone of eastern Iran. Geol Soc Am Bull 94: 134-156.

Vervoort JD, Patchett PJ, Blichert-Toft J, Albarede F (1999). Relationship between Lu–Hf and Sm–Nd isotopic systems in the global sedimentary system. Earth Planet Sc Lett 168: 79-99.

Wang K, Plank T, Walker JD, Smith EI (2002). A mantle melting profile across the Basin and Range, SW USA. J Geophys Res 107: 5-21.

Whitney DL, Evans BW (2010). Abbreviations for names of rock-forming minerals. Am mineral 95: 185-187.

Wilson M, (1989). Igneous Petrogenesis. London, UK: Chapman and Hall.

Winter J (2001). Introduction to Igneous and Metamorphic Petrology. Upper Saddle River, NJ, USA: Prentice Hall.

Zarrinkoub MH, Pang KN, Chung SL, Khatib MM, Mohammadi SS, Chiu HY, Lee HY (2012). Zircon U-Pb age and geochemical constraints on the origin of the Birjand ophiolite, Sistan suture zone, eastern Iran. Lithos 154: 392-405.

Zirjanizadeh S, Karimpour MH, Nasrabadi KE, Santos JF (2016). Petrography, Geochemistry and Petrogenesis of Volcanic Rocks, NW Ghonabad, Iran. J Econ Geol 8: 265-282.

Zulkarnain I (2009). Geochemical signature of Mesozoic volcanic and granitic rocks in Madina regency area, North Sumatra, Indonesia and its tectonic implication. Indonesian J Geosci 4: 117-131.